An Improved Temperature and Emissivity Separation Algorithm for the Advanced Himawari Imager

Shugui Zhou and Jie Cheng, *Senior Member, IEEE*

***Abstract*— This study proposes an improved temperature and emissivity separation (TES) algorithm for simultaneously retrieving the land surface temperature and emissivity (LST&E) from the Advanced Himawari Imager (AHI) data, including a modified water vapor scaling (WVS) method and a calibrated empirical relationship over vegetated surfaces. The modified WVS algorithm is comparable to the original WVS algorithm in deriving the LST&E but expands the application scope of the original WVS algorithm. The calibrated empirical relationship improved the LST&E and retrieval accuracy over vegetated surfaces by up to 0.165 K and 0.004, respectively. Comprehensive validation and evaluation are conducted in this study. *In situ* measurements from three networks are collected for the temperature-based validation. The bias and RMSE are 0.19 and 2.93 K in the daytime, and −0.43 and 1.95 K in the nighttime, respectively. Radiance-based LST validation shows that the bias and RMSE are 0.25 and 1.88 K, respectively. In addition, the AHI LST is evaluated using the MYD11 LST over large inland lakes, and the bias and RMSE are 0.25 and 1.12 K, respectively. The AHI LST is also compared to the MYD21 LST. The spatial distributions of the two LSTs are similar, and the LST differences are mostly within 4 K. The bias of the AHI LST ranges from −0.57 to 0.36 K, and the RMSE ranges from 1.7 to 2.64 K. The retrieved AHI LSE is compared with the latest MYD21 LSE. The biases and RMSEs are smaller than 0.005 and 0.014, respectively, for the three AHI bands. The improved TES algorithm is proven to be capable of obtaining accurate LST and LSE from AHI data.**

***Index Terms*— Advanced Himawari Imager (AHI), Himawari-8, land surface emissivity (LSE), land surface temperature (LST), temperature and emissivity separation (TES), thermal infrared (TIR).**

I. Introduction

THE land surface temperature (LST), as a significant parameter of land surface processes, is a direct driving factor of surface–atmosphere energy exchange [1]–[5]. It is of great significance to numerical weather prediction and climate change, surface energy balance, drought monitoring, urban heat islands, ocean circulation, and many other research fields [6]–[8].

Generally, there are two ways to obtain the LST – ground monitoring and satellite remote sensing. The accuracy of field measurements is high with a good temporal continuity that is not affected by weather conditions, whereas the LST at the remote sensing pixel scale is affected by solar radiation, topographic relief, elevation, soil moisture, and surface vegetation cover. In addition, the spatial distribution of the surface temperature is nonuniform and varies over time. Due to the limited ground stations, it is impossible to effectively monitor the LST changes over a large area. Therefore, remote sensing has become an important method for obtaining large-scale LST.

Satellite retrieval of the LST dates back to the 1970s [9]. A large number of LST retrieval methods have been proposed for thermal infrared (TIR) data. These algorithms are divided into two categories according to whether extra atmospheric information is needed. For example, the atmospheric information is needed for the mono-window algorithm [10], generalized single-channel algorithm [11], [12], temperature and emissivity separation (TES) algorithm [13]–[18], temperature-independent spectral indices method [19], and Moderate Resolution Imaging Spectroradiometer (MODIS) day–night algorithm [20]. Although the MODIS day–night algorithm does not rely on additional atmospheric information for atmospheric correction, the shapes of atmospheric air temperature and water vapor profiles are needed. Other algorithms, e.g., the generalized split-window algorithm [21], multichannel LST inversion algorithm [22]–[24], and multiangle LST inversion algorithm [22], [25], can conduct atmospheric correction using atmospheric absorption differences of different angles or channels. Due to the advancement of hyperspectral TIR sensors, many land surface temperature and emissivity (LST&E) retrieval algorithms have also been developed, such as hyperspectral TES algorithms [26]–[29] and physical-based integrated inversion algorithms [30], [31]. Among all methods mentioned above, the split-window algorithm is the most robust and widely used method and has been successfully applied to a variety of sensors for the production of operational LST products, e.g., MODIS [21], [32], VIIRS [33], SEVIRI [34], FY-2C [35], FY-3A [36], and GOES series [37].

The Himawari-8 is the successor of MTSAT-2 and was launched in July 2015. Himawari-8's status as the world's first next-generation satellite has made it a subject of global

Manuscript received January 5, 2020; revised February 17, 2020; accepted March 7, 2020. Date of publication March 31, 2020; date of current version September 25, 2020. This work was supported in part by the Second Tibetan Plateau Scientific Expedition and Research Program (STEP) under Grant 2019QZKK0206, in part by the National Natural Science Foundation of China under Grant 41771365, and in part by the National Key Research and Development Program of China under Grant 2016YFA0600101. *(Corresponding author: Jie Cheng.)*

The authors are with the State Key Laboratory of Remote Sensing Science, Jointly Sponsored by Beijing Normal University and the Institute of Remote Sensing and Digital Earth, Chinese Academy of Sciences, Beijing 100875, China, and also with the Institute of Remote Sensing Science and Engineering, Faculty of Geographical Science, Beijing Normal University, Beijing 100875, China (e-mail: jie_cheng@bnu.edu.cn).

Color versions of one or more of the figures in this article are available online at http://ieeexplore.ieee.org.

Digital Object Identifier 10.1109/TGRS.2020.2979846

attention and keen anticipation [38]. The Advanced Himawari Imager (AHI) onboard the Himawari-8 has four TIR channels located in the atmospheric window and views the Earth every ten minutes, which opens up new opportunities for the research of daily LST variations and the land surface energy balance.

Clearly, the Himawari-8 does not yet provide an official LST product. One of the primary reasons is that we do not have an effective algorithm, which means that the current LST retrieval algorithms mentioned above have limitations. Since the LST&E are coupled, the land surface emissivity (LSE) needs to be determined prior to the application of LST retrieval algorithms such as the split-window and single-channel algorithms. The widely used classification-based LSE assigning method cannot reflect seasonal variations in emissivity and has problems over semiarid and barren areas [39]–[41]. The multitemporal algorithm, such as the MODIS day–night algorithm, assumes that the LSE is unchanged for the same pixel within a short time, which is unreasonable due to abrupt weather changes and pixel mismatches at the global scale. The accuracy of LST&E obtained by the TES algorithm relies on the accuracy of atmospheric correction. Incomplete atmospheric correction will cause large uncertainties in the retrieved LST&E [42]. In summary, it is necessary to develop a practical and physical-based algorithm that considers the instrument characteristics of the AHI to obtain LST&E from the AHI.

The AHI has four TIR channels located in the atmospheric window, which is adapted to retrieve the LST&E simultaneously using the TES algorithm. To improve the accuracy of atmospheric correction, the water vapor scaling (WVS) method proposed by Tonooka [43], [44] is a good choice, which has been integrated into the MODIS and VIIRS TES algorithms [16], [18]. According to [42], [45], and [46], the WVS algorithm significantly reduced the LST&E estimation uncertainties in the TES algorithm. The uncertainty of LST estimation was reduced from 3.1 to 1.2 K for the Advanced Spaceborne Thermal Emission and Reflection Radiometer (ASTER) based on tests over a wide range of representative simulated data [42].

In this article, we have developed an improved TES algorithm for obtaining clear-sky LST&E from AHI data. The structure of the article is arranged as follows. The detailed information about the Himawari-8/AHI data is provided in Section II. The theoretical basis of the TES and modified WVS algorithms are described in Section III. Section IV presents the T-based and Radiance-based (R-based) validation results of the derived AHI LST as well as the cross-validation results of the AHI LST&E. A short discussion and conclusion are given in Sections V and VI, respectively.

II. Himawari-8/AHI

The Himawari-8 geostationary meteorological satellite began operation in July 2015, which covers the East Asia and Western Pacific regions (60° N∼60° S, 80° E∼160° W) with a longitude of 140.7° E. The observation cycle of the Himawari-8 is 10 min for a full disk, which has higher spatial and temporal resolutions compared to those of previous geostationary satellites MTSat-2 (Himawari-7). The AHI/Himawari-8 has 16 bands operating in the VIS (three bands), near infrared response (NIR) (three bands), and infrared (ten bands) spectral bands with spatial resolutions ranging from 0.5 to 2 km. Detailed information about the TIR bands of the AHI is provided in Table I.

TABLE I
AHI Instrument Specifications for the TIR Bands

AHI band	Central wavelength (μm)	Spatial resolution (km) at the nadir	Remark
11	8.5	2	Atmospheric windows
12	9.61	2	Ozone
13	10.31	2	Atmospheric windows
14	11.2	2	Atmospheric windows
15	12.3	2	Atmospheric windows
16	13.3	2	Carbon dioxide

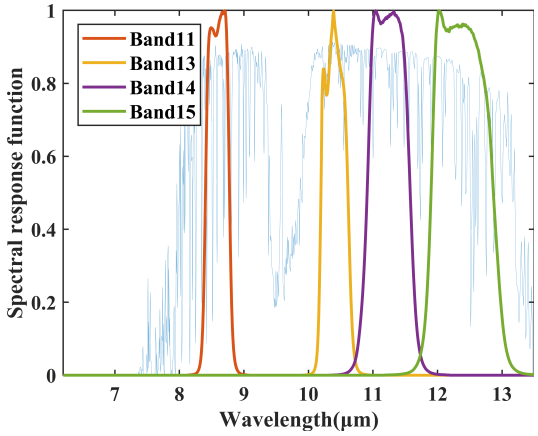

Fig. 1. Spectral response functions of the four AHI TIR bands (bands 11, 13, 14, and 15). The blue dotted line shows the atmospheric transmittance of the 1976 standard atmosphere.

Because bands 12 and 16 are located in the ozone and carbon dioxide absorption zones, respectively, TIR bands 11 and 13–15 are adopted in the improved TES algorithm. The corresponding band response functions of the four bands are shown in Fig. 1.

III. Theoretical Basis

A. TES Algorithm

Under the assumption that the land surface is a Lambertian and atmospheric correction is conducted accurately, the ground-leaving radiance can be expressed as follows:

$$L_\lambda(\theta) = \varepsilon_\lambda B_\lambda(T_s) + (1-\varepsilon_\lambda)\overline{L_{\text{atm}\downarrow,\lambda}} \tag{1}$$

where $L_\lambda(\theta)$ is the ground-leaving radiance, λ is the wavelength, θ is the view zenith angle, ε_λ is the LSE at wavelength λ, T_S is the LST, and $B_\lambda(T_s)$ is the Planck function. $\overline{L_{\text{atm}\downarrow,\lambda}}$ is the equivalent atmospheric downward radiance, which can be simulated using the radiative transfer

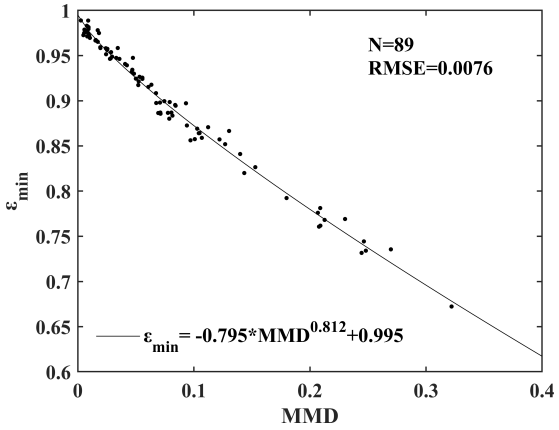

Fig. 2. Empirical relationship between $\varepsilon_{\min}$ and MMD for the AHI. Dots correspond to the samples used to fit the relationship, and continuous line is the fitted relationship. N is the number of the samples.

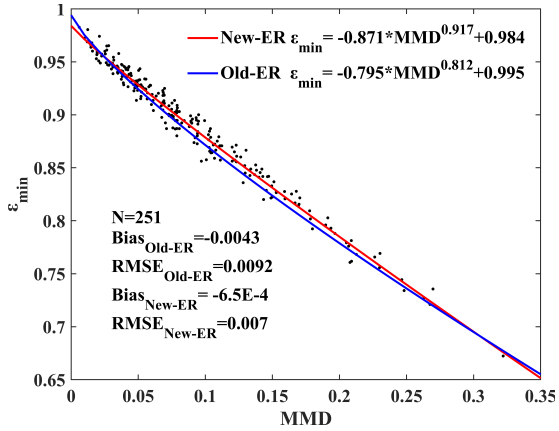

Fig. 3. Comparison between the calibrated and original empirical relationships for the AHI (Old-ER is the original empirical relationship, and New-ER is the calibrated empirical relationship).

model such as moderate resolution atmospheric transmission (MODTRAN 5.2) model [47]. The equation for separating the LST&E is underdetermined, and additional constraints must be imposed to better pose the underdetermined equations. Taking the typical TES algorithm as an example, an empirical relationship between the minimum emissivity and emissivity contrast is used to constrain the emissivity shape [13], [48].

The TES algorithm was originally proposed for the ASTER [13], which consists of three parts.

1) The normalized emissivity method (NEM) module is used to obtain the initial LST value and the LSE spectrum by iteratively eliminating the equivalent atmospheric downward radiance [49].
2) *Ratio Model*: Emissivities are ratioed to their mean values to obtain the LSE spectrum shape but not the actual emissivities.
3) *Maximum-Minimum Difference (MMD) Module*: The empirical relationship between the minimum emissivity $\varepsilon_{\min}$ and the spectral contrast MMD is established to obtain the refined LSE and recover the amplitude of the LSE spectrum [50], [51].

The empirical relationship between $\varepsilon_{\min}$ and MMD is usually established using the emissivity spectra chosen from the ASTER spectral library to represent natural scenes. Specific details of the TES algorithm can be found in [13].

In this article, the empirical relationship of the TES algorithm is constructed using 89 ASTER emissivity spectra, including rocks, soils, water, vegetation, and ice/snow [52]. These emissivity spectra are then convoluted with the band response functions of the AHI, accordingly, to obtain the band emissivity. The coefficient of the empirical relationship is fitted using the least squares method, and the result is shown in Fig. 2

$$\varepsilon_{\min} = -0.795 \times \mathrm{MMD}^{0.812} + 0.995. \tag{2}$$

During construction of the empirical relationship, pure soil/leaf emissivity spectra are considered. Multiple scattering in the real soil–vegetation system (the cavity effect) is neglected, leading to the emissivity underestimation of vegetated surfaces in the original TES algorithm [53], [54]. To incorporate the cavity effect, we recalibrate the empirical relationship using the canopy directional emissivity spectra simulated by the 4SAIL model [55].

To compute the vegetation canopy emissivity, the parameters listed below are fed into 4SAIL: 1) the optical properties of the vegetation canopy: leaf emissivity and soil emissivity; 2) leaf area index (LAI); 3) view zenith angle; and 4) leaf inclination distribution function (LIDF) parameter. Fifteen leaf emissivity spectra and 69 soil emissivity spectra were extracted from the MODIS University of California, Santa Barbara (UCSB) emissivity library (https://icess.eri.ucsb.edu/modis/EMIS/html/em.html) and the ASTER emissivity library [52]. The LAI varies from 0 (bare soil) to 7 (dense vegetation cover), with an interval of 0.5. The differences between 4SAIL-modeled directional emissivity using four different LIDFs are less than 0.005 according to Verhoef *et al.* [55]. Therefore, the LIDF is set as spherical distribution function in this study. The view zenith angle ranges from 0° to 65°, with an interval of 15°. The spectral interval and resolution were set to 714–1250 and 1 cm^{-1}, respectively. To reduce emissivity spectra redundancies, we screened out the 4SAIL output emissivity spectra with similar spectral behaviors using the spectral angle mapper (SAM) algorithm [56]. Finally, 251 spectra were retained and used to recalibrate the empirical relationship for vegetated surfaces. The fitted new relationship for vegetated surfaces is shown in (3). A comparison between the new empirical relationship obtained with 4SAIL simulations and the original empirical relationship constructed with pure emissivity spectra is shown in Fig. 3. Fig. 3 reveals that the original empirical relationship underestimates the $\varepsilon_{\min}$, especially when MMD is between 0.05 and 0.25

$$\varepsilon_{\min,\mathrm{veg}} = -0.871^{*}\mathrm{MMD}^{0.917} + 0.984. \tag{3}$$

According to [57], when the atmospherically corrected MODIS normalized difference vegetation index (NDVI) is smaller than 0.156, the pixel can be regarded as bare soil. When the MODIS NDVI is larger than 0.156 and smaller than 0.461, the pixel is treated as partially vegetated land, and

when the NDVI is larger than 0.461, the pixel is identified as fully vegetated. Therefore, for pixels with NDVI $>$ 0.156, the calibrated empirical relationship is adopted in the TES; otherwise, the original TES empirical relationship is preferred.

B. Atmospheric Correction

The accuracy of the atmospheric correction depends on the atmospheric profiles (primarily the atmospheric temperature and water vapor mixing ratio profiles) we can obtain. The radiosonde technique is the most accurate way to obtain atmospheric temperature and water vapor profiles [58]. However, radiosonde observations are conducted at several fixed times each day (00:00 and/or 12:00 UTC), and cannot be used at large scales. Therefore, various types of atmospheric profile products are used as alternatives for atmospheric correction. In this article, 6-h pressure-level-analyzed meteorological files of the Modern-Era Retrospective analysis for Research and Applications, version 2 (MERRA-2) [59] are selected for the AHI atmospheric correction, which can be downloaded from https://disc.sci.gsfc.nasa.gov/daac-bin/FTPSubset2.pl. MERRA-2 contains vertical parameters including the air temperature, geopotential height, and specific humidity at 42 pressure levels ranging from 1000 to 0.1 hPa.

The atmospheric water vapor content changes greatly and has a great impact on atmospheric correction for AHI TIR bands. Residual errors due to incorrect atmospheric correction in the TES algorithm give rise to large uncertainties in the obtained LST&E [42], [60]. Therefore, a modified WVS algorithm is implemented to improve the atmospheric correction accuracy for the AHI. Unlike WVS algorithm, which is only applied to the graybody pixels, and the scaling factors of nongraybody pixels are interpolated from the scaling factors of the neighboring graybody pixels, the modified WVS algorithm is extended to nongraybody pixels by fitting the coefficients of the extension of the multichannel water vapor dependent (EMC/WVD) algorithm according to the minimum emissivity of the AHI bands.

The WVS method originally proposed by Tonooka [43], [44] is used to improve the atmospheric correction accuracy, which has been integrated into the production of remote sensing LST&E products, e.g., MODIS [61] and VIIRS [16].

The WVS algorithm is an EMC/WVD algorithm [62]. The EMC/WVD algorithm models the at-surface brightness temperature using the top of the atmosphere (TOA) brightness temperature and the total precipitable water (TPW)

$$\begin{aligned} T_{g,i} &= \alpha_{i,0} + \sum_{k=1}^{n} \alpha_{i,k} T_k \\ \alpha_{i,k} &= p_{i,k} + q_{i,k} W + r_{i,k} W^2, \quad (k = 1, , , n) \end{aligned} \tag{4}$$

where W is the TPW; $T_{g,i}$ is the at-surface brightness temperature; T_k is the at-sensor brightness temperature for band k; $\alpha_{i,0}$, $\alpha_{i,k}$, $p_{i,k}$, $q_{i,k}$, and $r_{i,k}$ are coefficients; i is the band number; and n is the number of bands. The coefficient of the EMC/WVD algorithm can be derived from simulated data. Assuming the atmospheric transmissivity τ can be expressed by the Pierluissi double exponential band model [63], the water vapor profile scaling factor γ can be calculated using the following equation:

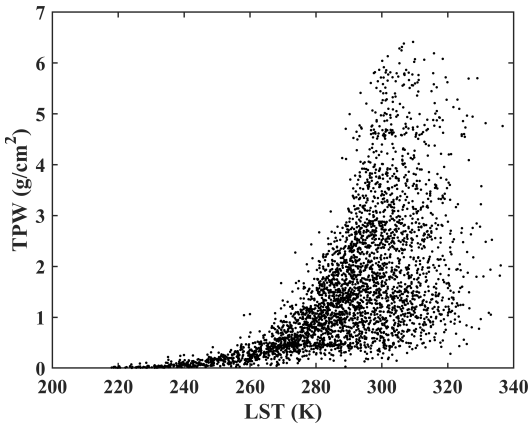

Fig. 4. Distribution of the LST with respect to the TPW for the profiles used in the simulation.

$$\gamma_i = \left(\frac{\ln\left(\frac{\tau_i(\theta,\gamma_2)^{\gamma_1^a}}{\tau_i(\theta,\gamma_1)^{\gamma_2^a}} \cdot \frac{B(T_{g,i}) - \frac{I_i^{\uparrow}(\theta,\gamma_1)}{1-\tau_i(\theta,\gamma_1)}}{I_{TOA,i} - \frac{I_i^{\uparrow}(\theta,\gamma_1)}{1-\tau_i(\theta,\gamma_1)}} \right)^{\left(\gamma_1^{a_i} - \gamma_2^{a_i}\right)}}{\ln\left(\frac{\tau_i(\theta,\gamma_2)}{\tau_i(\theta,\gamma_1)} \right)} \right)^{1/a_i} \tag{5}$$

where a_i is the band model parameter; γ_1 and γ_2 are two appropriately chosen scaling values; $\tau_i(\theta, \gamma_1)$ is the atmospheric transmissivity with the atmospheric water vapor profile scaled by γ_1; $I_i^{\uparrow}(\theta, \gamma_1)$ is the atmospheric upwelling radiance with the water vapor profile scaled by γ_1; γ_1 and γ_2 are set as 1.0 and 0.7, respectively.

1) EMC/WVD Coefficients: The coefficients of the EMC/WVD method are determined by the training data, which are constructed using the radiation transfer model with representative atmospheric profiles extracted from the SeeBor V5.0 database and representative emissivity spectra selected from ASTER and MODIS spectral libraries. For details about SeeBor, please refer to [64]. The atmospheric profiles over the ocean are excluded first, and the left atmospheric profiles are filtered with the following criteria to eliminate possible cloudy atmospheric profiles, i.e., the relative humidity must be lower than 90% at each pressure level [64]. Finally, 3517 atmospheric profiles are selected from SeeBor, and the distribution of the LST with respect to the TPW for the selected atmosphere profiles is shown in Fig. 4.

In total, 198 emissivity samples, including a variety of materials such as water, snow/ice, vegetation, soils, sands, and rock, are selected from the ASTER and MODIS spectral libraries, with the emissivity ranging from 0.65 to 1 (Fig. 5).

The emissivity spectra are then convolved with the AHI's spectral response function (four bands: M11, M13, M14, and M15). The LST–surface air temperature differences (δLST) are set as -10, -5, 0, 5, 10, and 15 K for each atmospheric profile. A total of 4 178 196 simulations (3517 profiles $\times$198 samples $\times$6δLST) are generated with the MODTRAN radiative transfer model for each view angle (0°, 15°, 30°, 45°, 60°, and 75°), and for the four AHI TIR bands. The simulated

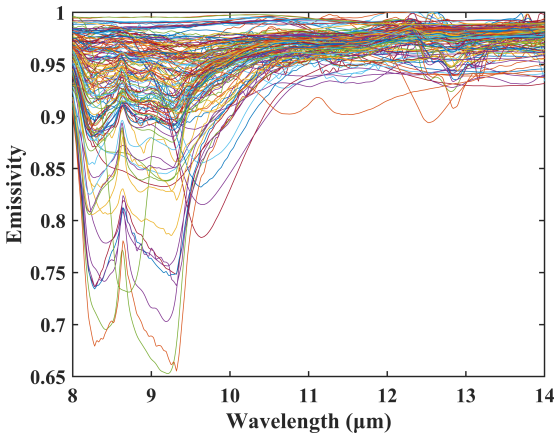

Fig. 5. Combination of MODIS and ASTER library emissivity spectra used for the development of the EMC/WVD algorithm.

data are divided into six groups according to the minimum band emissivity: [0.96,1], [0.91,0.96], [0.86,0.91], [0.81,0.86], [0.76,0.81], and [0.71,0.76] for each view angle. Using the simulated TOA brightness temperature, ground-leaving brightness temperatures, and the TPW of each atmosphere profile, the coefficients in (4) are derived using the least squares method. The EMC/WVD algorithm coefficients are determined by the view zenith angle and minimum band emissivity.

To determine the minimum band emissivity and the EMC/WVD algorithm coefficients, we need to identify the gray pixels first. If all the band emissivities are higher than 0.96, e.g., water, snow/ice, and dense vegetation, then the pixel is labeled as a graybody pixel. The MODIS 16-day synthetic NDVI product (MOD13A2) after reconstruction by the Savitzky–Golay filter algorithm [65] is also used to identify gray pixels. When NDVI >0.3, the pixel is labeled as a gray pixel. Furthermore, MODIS snow product MOD10A2 is used to identify water and snow cover pixels. For the other AHI pixels, the minimum band emissivity is determined using the combined ASTER and MODIS emissivity for land (CAMEL) emissivity product [66], [67]. The CAMEL data set was created by combining the University of Wisconsin–Madison MODIS infrared emissivity data set and the Jet Propulsion Laboratory ASTER global emissivity data set version 4. Details about the CAMEL data set can be found from the website: https://lpdaac.usgs.gov/products/cam5k30emv002/. The spatial resolution of CAMEL data is 0.05°. The CAMEL data is resampled to 0.02° using the nearest neighbor interpolation. Regarding the spectral matching, we first establish the linear relationship between AHI channel emissivity and the corresponding CAMEL channel emissivity using the 89 emissivity spectra in Section III. Then the CAMEL channel emissivities are converted to AHI channel emissivities using the established linear relationships. After the minimum band emissivity of each pixel is determined, the EMC/WVD coefficients are assigned according to the view angle, and then the ground-leaving brightness temperature is calculated using (4). When the view zenith angle is not equal to the specified angles (0°, 15°, 30°, 45°, 60°, or 75°), the at-surface brightness temperature is linearly interpolated from the values at the adjacent view zenith angles.

TABLE II
VALUE OF BAND MODEL A FOR EACH BAND

Band	Coefficient a_i	RMSE of γ (γ=0.9)
11	1.4310	0.000431
13	1.8649	0.000154
14	1.8333	0.000238
15	1.7343	0.000470

TABLE III
REGRESSION COEFFICIENTS OF (7)

Band	a	b	c	RMSE(W/cm^2/sr/cm^{-1})
11	1.7103E-08	1.74642	-76366.386	6.274E-08
13	5.0492E-08	1.73243	-66474.210	4.874E-08
14	6.0151E-08	1.70345	-55013.860	6.881E-08
15	9.5320E-08	1.64039	-40117.495	1.316E-07

The band model coefficients a_i in (5) are determined using simulated data, where γ, γ_1, and γ_2 are set as 0.9, 0.7, and 1, respectively. The values of the band model coefficients are listed in Table II.

2) Estimation of the Atmospheric Downward Radiance: The initial atmospheric parameters, $\tau_i(\theta)$, and $I_i^{\uparrow}(\theta)$, are estimated using Radiative Transfer for TOVS 12 (RTTOV) [68]. The input atmospheric profiles (air temperature and water vapor mixing ratio profiles) are extracted from the MERRA-2 product. Given that the water vapor profile scaling factor γ has been estimated using (5), γ is then used to scale $\tau_i(\theta)$ and $I_i^{\uparrow}(\theta)$ for each pixel as follows:

$$\tau_i(\theta,\gamma) = \tau_i(\theta,\gamma_1)^{\frac{\gamma a_i-\gamma_2 a_i}{\gamma_1 a_i-\gamma_2 a_i}} \cdot \tau_i(\theta,\gamma_2)^{\frac{\gamma_1 a_i-\gamma a_i}{\gamma_1 a_i-\gamma_2 a_i}}$$
$$L_i^{\uparrow}(\theta,\gamma) = L_i^{\uparrow}(\theta,\gamma_1)\frac{1-\tau_i(\theta,\gamma)}{1-\tau_i(\theta,\gamma_1)}. \quad (6)$$

The equivalent downward atmospheric radiance, $I_i^{\downarrow}$, is estimated using the following nonlinear equation of the atmospheric upwelling radiance at the nadir view, $I_i^{\uparrow}(0,\gamma)$ [69]:

$$I_i^{\downarrow}(\gamma) = a_i + b_i I_i^{\uparrow}(0,\gamma) + c_i I_i^{\uparrow}(0,\gamma)^2 \quad (7)$$

where a_i, b_i, and c_i are regression coefficients, which can be derived using the least squares method with SeeBor atmospheric profiles. The atmospheric upwelling radiance at the nadir view $I_i^{\uparrow}(0,\gamma)$ is calculated from $\tau_i(\theta,\gamma)$ and $I_i^{\uparrow}(\theta,\gamma)$ at view angle θ [69]

$$I_i^{\uparrow}(0,\gamma) = I_i^{\uparrow}(\theta,\gamma)\frac{1-\tau_i(\theta,\gamma)^{\cos\theta}}{1-\tau_i(\theta,\gamma)}. \quad (8)$$

The regression coefficients of (7) for channels 11 and 13–15 are summarized in Table III. The scatterplot between the path radiance at the nadir view and downward sky radiance is shown in Fig. 6.

As shown in Fig. 6, the accuracy of this equation is relatively high, with an RMSE less than 1.32E-07 W/cm^2/sr/cm^{-1}.

TABLE IV
INFORMATION OF SITES IN THE OZFLUX, BSRN, AND HIWATER NETWORKS

Network	Site name	Latitude	Longitude	Land cover	Instrument
OzFlux	Ashley Dene	-43.64405°	172.3547°	cropland	Hukseflux R01
	CapeTribulation	-16.10322°	145.4469°	shrub-land	Kipp & Zonen CNR4
	Dry River	-15.2588°	132.3706°	open forest savanna	Kipp & Zonen CNR4
	Robson Creek	-17.11747°	145.6301°	forest	Hukseflux NR01
	Samford	-27.38806°	152.8778°	pasture	Kipp & Zonen CNR1
	Warra	-43.09502°	146.6545°	forest	Kipp & Zonen CNR4
BSRN	TAT	36.0581°	140.1258°	grassland	Kipp & Zonen CGR4
HiWATER	AR	38.0473°	100.4643°	savanna and grassland	CNR1 net radiometers
	DM	38.8555°	100.3722°	maize	CNR1 net radiometers
	EB	37.9492°	100.9151°	alpine meadow	CNR1 net radiometers
	DSL	38.8399°	98.9406°	marsh alpine meadow	CNR1 net radiometers
	SDQ	42.0012°	101.1374°	tamarix	CNR1 net radiometers
	HZZ	38.7652°	100.3186°	barren land	CNR1 net radiometers
	HM	42.1135°	100.9872°	barren land	CNR1 net radiometers

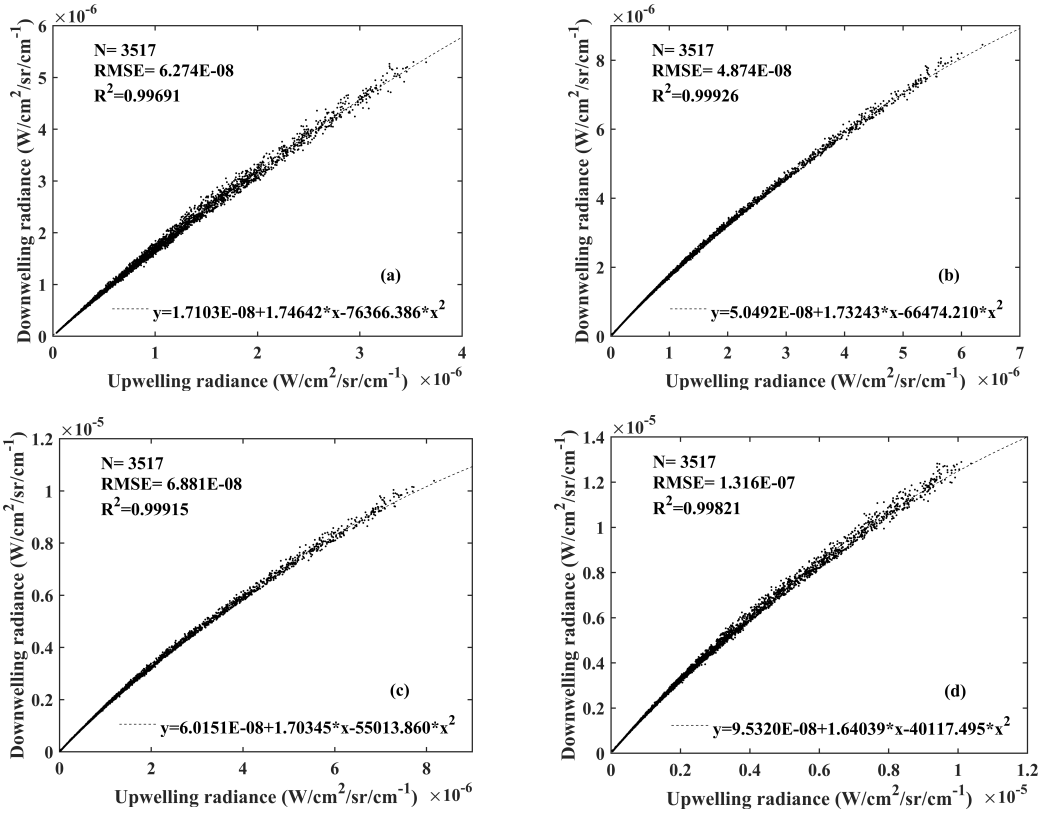

Fig. 6. Scatterplot of the atmospheric upwelling and downwelling radiance for the four AHI bands. (a) Band 11. (b) Band 13. (c) Band 14. (d) Band 15.

C. Implementation of the Improved TES Algorithm

Fig. 7 shows the flowchart of the improved LST&E retrieval algorithm which consists of two components: atmospheric correction and LST&E separation. Atmospheric correction is conducted using the modified WVS algorithm, which can improve the accuracy of atmospheric correction, especially under humid atmospheric conditions. The calibrated empirical relationship is used for vegetated surfaces in the simultaneous retrieval of the LST&E.

IV. RESULTS

To evaluate the accuracy of the AHI LST&E derived by the improved TES algorithm, a comprehensive validation is

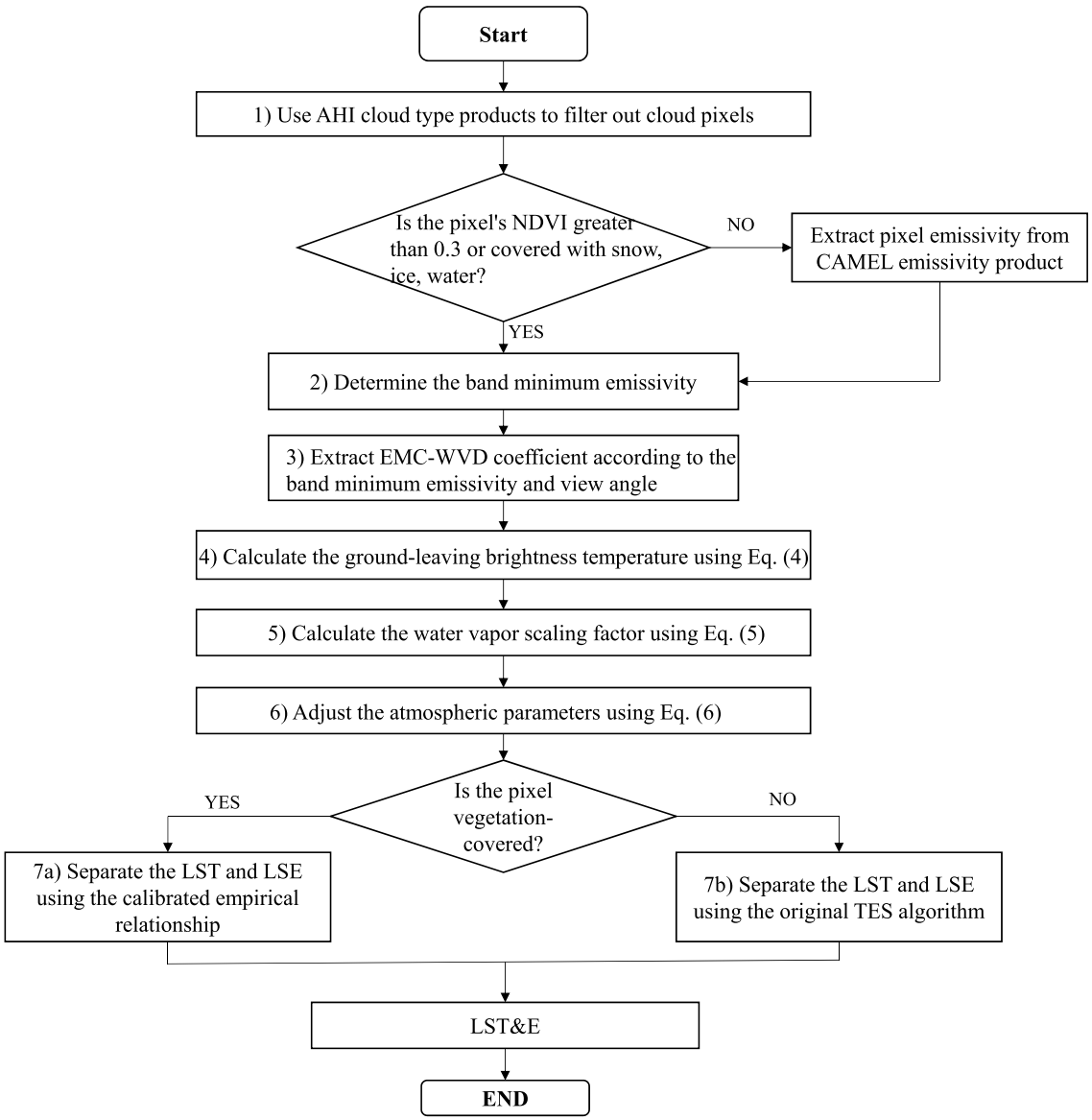

Fig. 7. Flow diagram showing all steps in retrieving the Himawari-8/AHI LST and LSE.

conducted, including temperature-based (T-based) validation, R-based validation, and cross-validation. First, the retrieved LSTs from the AHI are validated using *in situ* measurements collected from three networks. Second, the R-based method is used to validate the AHI LST at sites with radiosonde measurements. Third, the AHI LST is compared to the MODIS LST product (MYD11 L2) with the same overpass time over several lakes. Fourth, the spatial distributions of the AHI and MODIS (MYD21 L2) LSTs are compared. Regarding the LSE, we compared the AHI-derived LSE with the MODIS MYD21 L2 LSE product.

A. T-Based Validation

One-year-old AHI TOA brightness temperature data and cloud type products (January 1, 2016–December 31, 2016) are used in this study. To reduce the data storage capacity, AHI data with a 1-h temporal resolution in the daytime and data with a consistent overpass time, similar to that of MODIS in the nighttime, are downloaded. As the AHI has no cloud mask product, the AHI cloud type product is used to identify the clear-sky pixels in the daytime instead; the MYD35 cloud mask product is used for cloud detection for the AHI, with the same observation time (less than 5 min) as that of MODIS in the nighttime.

Details of the validation sites in the Heihe Watershed Allied Telemetry Experimental Research (HiWATER, http://card.westgis.ac.cn/) network [70], [71], Baseline Surface Radiation Network (BSRN, https://bsrn.awi.de/) [72], and OzFlux (http://www.ozflux.org.au/) [73] network are summarized in Table IV.

The spatial resolution of AHI pixels is 0.02°, whereas the footprint of the *in situ* measurement is much smaller than that of the AHI. Five years (2013–2017) of the ASTER AST08 LST product are collected to evaluate the heterogeneity of the *in situ* measurements before they are used

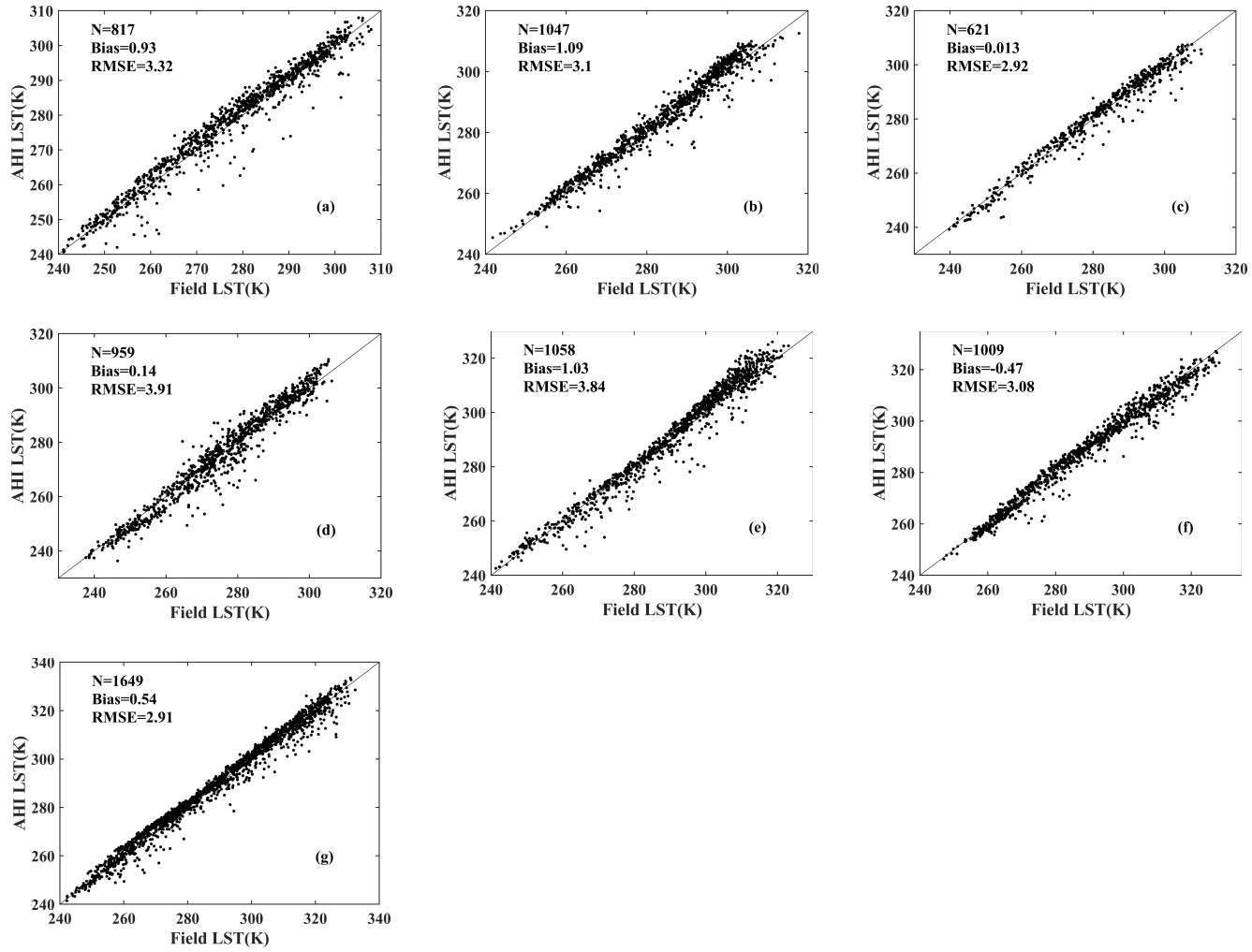

Fig. 8. AHI LST validation results with respect to the HiWATER sites in the daytime. (a) A'rou (AR). (b) Daman (DM). (c) E'bao (EB). (d) Dashalong (DSL). (e) Sidaoqiao (SDQ). (f) Huazhaizi (HZZ). (g) Huangmo (HM).

for AHI LST validation. We calculate the standard deviations (STDs) of the ASTER LSTs in 2 km × 2 km windows around sites and determine that the STDs are less than 2 K in most cases. Therefore, the *in situ* measurements can be directly used for AHI LST validation. The details of the mean, minimum, and maximum LST STDs are provided in Table V.

For the sites in the BSRN, HiWATER, and OzFlux networks, the LST is calculated from the measured surface upwelling and downward longwave radiation using the following equation:

$$T_s = \left(\frac{L^{\uparrow} - (1-\varepsilon)L^{\downarrow}}{\varepsilon \sigma} \right)^{1/4} \tag{9}$$

where T_s is the LST and ε is the surface broadband emissivity (BBE), which is obtained from MOD11B1 using the following equation [74]:

$$\varepsilon = 0.095 + 0.329 \times \varepsilon_{29} + 0.572 \times \varepsilon_{31}. \tag{10}$$

The uncertainty of the estimated BBE comes from two parts: one is the uncertainty in the spectral conversion, i.e., converting narrow band emissivity to BBE; and the other is the uncertainty of the MODIS land surface emissivity product. The RMSE of spectral conversion [see (10)] is 0.01 [74], and the RMSDs of MOD11B1 band 29 (8.52 μm) and 31 (11.03 μm) emissivities are 0.009 and 0.006, respectively, when compared to ASTER emissivity product [75]. Based on

TABLE V
LST VARIATION AT THE OZFLUX, BSRN, AND HIWATER SITES

Network	Site name	LST STD (K)		
		Mean	Minimum	Maximum
OzFlux	Ashley Dene	1.51	0.76	2.98
	CapeTribulation	1.83	0.57	3.96
	Dry River	1.03	0.41	1.80
	Robson Creek	1.20	0.47	2.26
	Samford	1.44	0.87	2.69
	Warra	0.72	0.59	0.83
BSRN	TAT	1.74	1.18	2.83
HiWATER	A`rou (AR)	1.07	0.59	1.90
	Daman (DM)	1.33	0.63	2.92
	E`bao (EB)	1.18	0.98	1.67
	Dashalong (DSL)	1.63	0.83	3.02
	Sidaoqiao (SDQ)	2.03	1.08	4.24
	Huazhaizi (HZZ)	0.98	0.44	3.14
	Huangmo (HM)	1.38	0.36	3.90

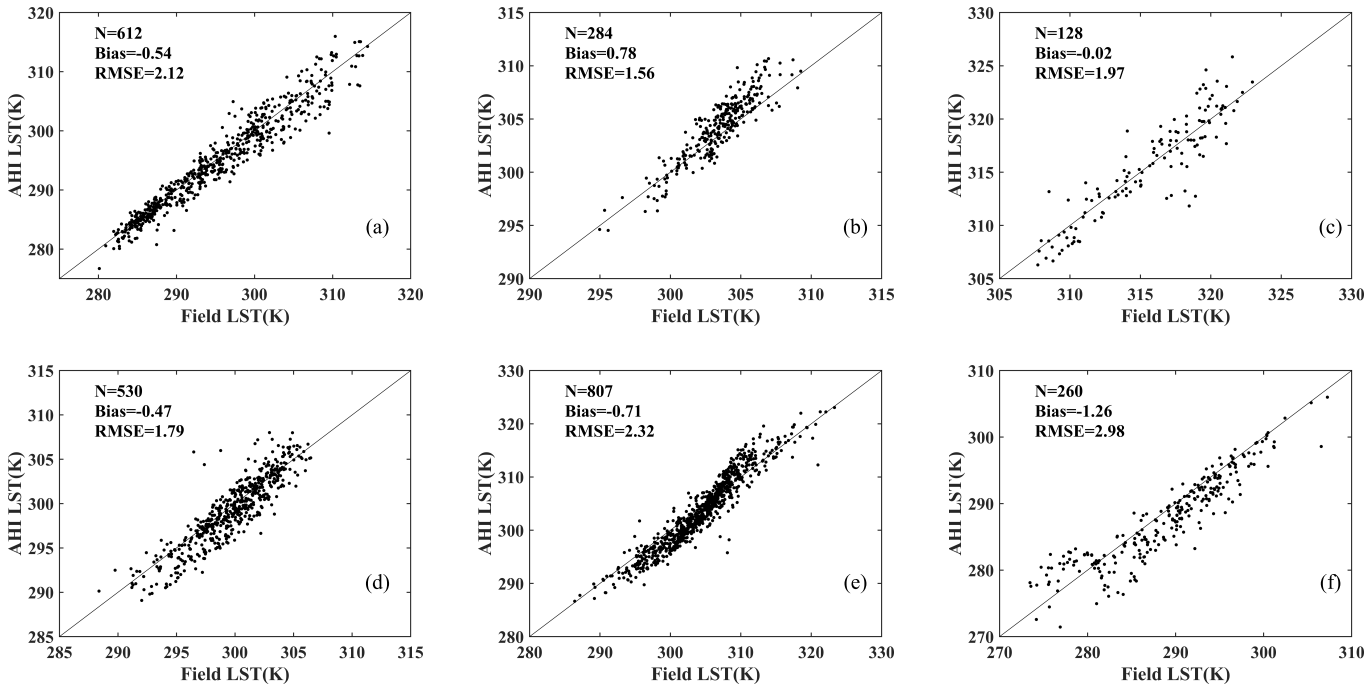

Fig. 9. AHI LST validation results with respect to the OzFlux sites in the daytime. (a) Ashley Dene. (b) CapeTribulation. (c) Dry River. (d) Robson. (e) Samford. (f) Warra.

the evaluation results of Hulley *et al.* [76], the mean emissivity differences between ASTER emissivity product and laboratory-measured emissivities are 1.87%, 1.16%, and 0.9% for ASTER bands 11 (8.6 μm), 13 (10.6 μm) and 14 (11.3 μm), respectively. The nominal accuracy of ASTER emissivity product is 0.015. Thus, the accuracy of ASTER bands 11, 13, and 14 are set to 0.019, 0.015, and 0.015, respectively. The uncertainty of MODIS band 29 is calculated as $(0.019^2 + 0.009^2)^{1/2} = 0.02$, and the uncertainty of MODIS band 31 is calculated as $(0.015^2 + 0.006^2)^{1/2} = 0.016$. Therefore, the uncertainty of BBE estimated by (10) is $\mathrm{sqrt}(0.01^2 + (\mathrm{sqrt}(0.329^2 * 0.02^2 + 0.572^2 * 0.016^2))^2) = 0.015$.

The measurement difference of all CNR1/CNR4 net radiometers ranged from approximately -8 to 3 W/m^2 (-8 W/m^2 in daytime and 3 W/m^2 at nighttime) compared with an Eppley Precision Infrared Radiometer during the HiWATER experiments [77]. The measurement difference of NR01 radiometer is less than 9.7 W/m^2 in daytime and 4.1 W/m^2 at nighttime [78].

Given that the surface longwave upwelling and downward radiation are equal to the global annual mean values of 397.5 and 339.7 W/m^2 [79], respectively, and the BBE is set to 0.95 with an uncertainty of 0.015, the uncertainty of LST calculated using (9) can be estimated using the error propagation law. LST uncertainty is equivalent to 1.62 and 0.37 K considering the measurement error of CNR1/CNR4 net radiometers, whereas the values are 1.58 and 0.57 K considering the measurement error of NR01 radiometer in daytime and nighttime, respectively.

The AHI LSTs were compared with the ground-measured LSTs, and scatterplots of the AHI and *in situ* LSTs are shown in Figs. 8–10.

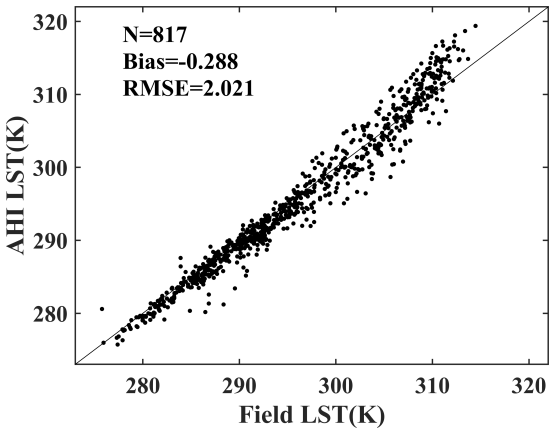

Fig. 10. AHI LST validation results with respect to the BSRN sites in the daytime.

For the seven sites in the HiWATER network during the daytime, the bias varies from -0.47 to 1.09 K, with an average of 0.51 K. The RMSE varies from 2.91 to 3.91 K, with an average of 3.31 K. For the six sites in the OzFlux network during the daytime, the bias varies from -1.26 to 0.78 K, with an average of -0.54 K. The RMSE varies from 1.56 to 2.98 K, with an average of 2.17 K. For one site in the BSRN network during the daytime, the bias and RMSE are -0.29 and 2.02 K, respectively. The RMSEs at the HiWATER sites are larger than those at the OzFlux and BSRN sites. One reason is that the AHI view zenith angle is approximately 60° at the HiWATER sites.

Since the AHI does not have cloud mask products in the nighttime, the MODIS cloud mask is used instead. Only AHI data with an observation time close to the overpass time of MODIS (within 10 min) is selected in the nighttime. The AHI

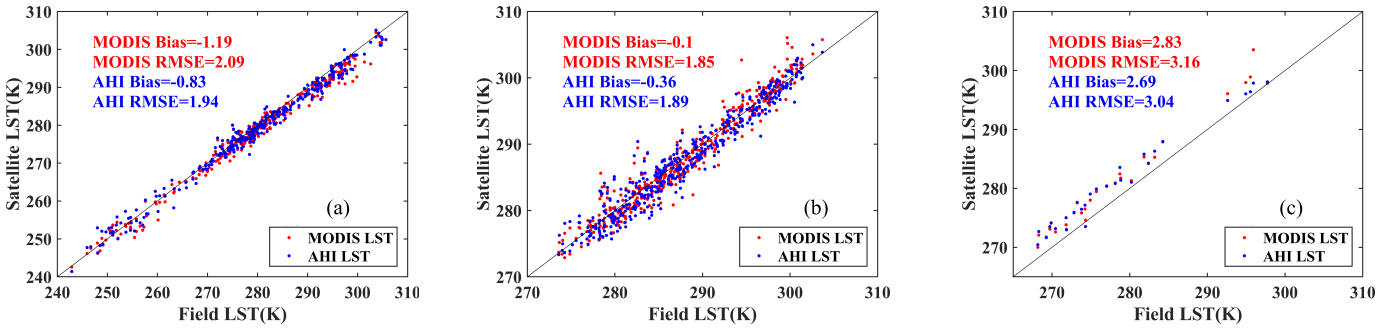

Fig. 11. AHI LST validation results at the (a) HiWATER, (b) OzFlux, and (c) BSRN sites during the nighttime.

and MYD21 LSTs are compared with the ground-measured LSTs, and scatterplots of the AHI and *in situ* LSTs are shown in Fig. 11. For the sites in the HiWATER network, the bias and RMSE are −0.83 and 1.94 K, respectively. The bias and RMSE of MODIS are −1.19 and 2.09 K, respectively. For the sites in the OzFlux network, the bias and RMSE are −0.36 and 1.89 K, respectively. The bias and RMSE of MODIS are −0.1 and 1.85 K, respectively. For the sites in the BSRN network, the bias and RMSE are 2.69 and 3.04 K, respectively. The bias and RMSE of MODIS are 2.83 and 3.16 K, respectively. As a result, similar accuracies were obtained for the AHI and MODIS, and the accuracy of the AHI was higher during the nighttime than that during the daytime, due to the lower heterogeneity of the surface temperature during the nighttime.

B. R-Based Validation

The R-based LST validation method was first proposed by Wan and Li [80], which only requires field measured LSE and synchronized atmospheric profiles. The R-based LST validation method has been applied to assess the satellite-derived LST products, such as MODIS [81], [82] and AIRS [83].

One-year-old (2016) radio sounding data, at 0000 UTC covering China and Australia, are downloaded from http://weather.uwyo.edu/upperair/sounding.html to implement the R-based AHI LST validation. Profiles with a low vertical resolution are eliminated (e.g., no observations above 400 hPa), and the relative humidity of each profile must be lower than 90% at each pressure level. The atmospheric profiles are input into MODTRAN 5.2 to calculate the atmospheric parameters. As band 14 (11.2 μm) has lower uncertainty in the LSE and is less sensitive to atmospheric absorption, the TOA brightness temperature of band 14 is selected to conduct the R-based LST validation.

The AHI LST is used as the initial value of the LST, and the emissivity of band 14 is estimated from the MOD11B1 band 31 emissivity by spectral conversion. The flowchart of R-based LST estimation is shown in Fig. 12. The R-based LST is then used for AHI LST validation.

Fig. 13 shows the locations of 31 sounding stations and the corresponding scatterplots of the AHI LST versus the R-based LST estimated from the AHI TOA radiances in band 14 over China and Australia. The bias and RMSE of the AHI LST

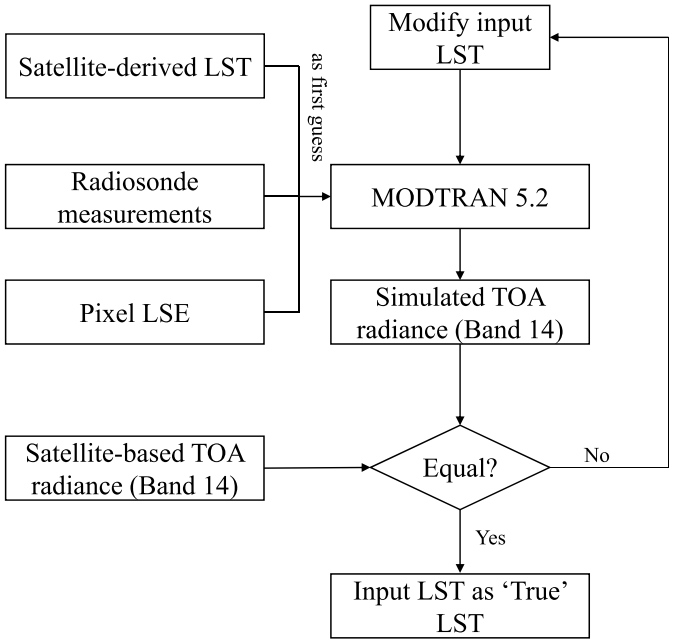

Fig. 12. Flowchart of R-based LST estimation.

are 0.274 and 1.918 K, respectively, for China and 0.018 and 1.438 K, respectively, for Australia.

C. Comparison With the MYD11 L2 LST

According to Wan *et al.* [84], the accuracy of the MODIS LST product derived by the split-window algorithm is higher than 1 K over lakes, when the TPW ranges from 0.4 to 3.0 g/cm^2. To further verify the AHI LST, we selected seven large inland lakes in China with the MODIS LST product covering these lakes. We compared the MODIS and AHI LSTs at the center of each lake under the condition that the TPW is lower than 3 g/cm^2, and the observation time difference between MODIS and AHI is less than 10 min. The specific locations of the lakes and the verification results are listed in Table VI and shown in Fig. 14, respectively. The bias and RMSE of this case are 0.25 and 1.12 K, respectively, compared with the MYD11L2 LST product.

D. Comparison With the MYD21 LST

The MODIS LST&E product, MYD21 V6, is also generated using the TES algorithm, the accuracy of which is higher

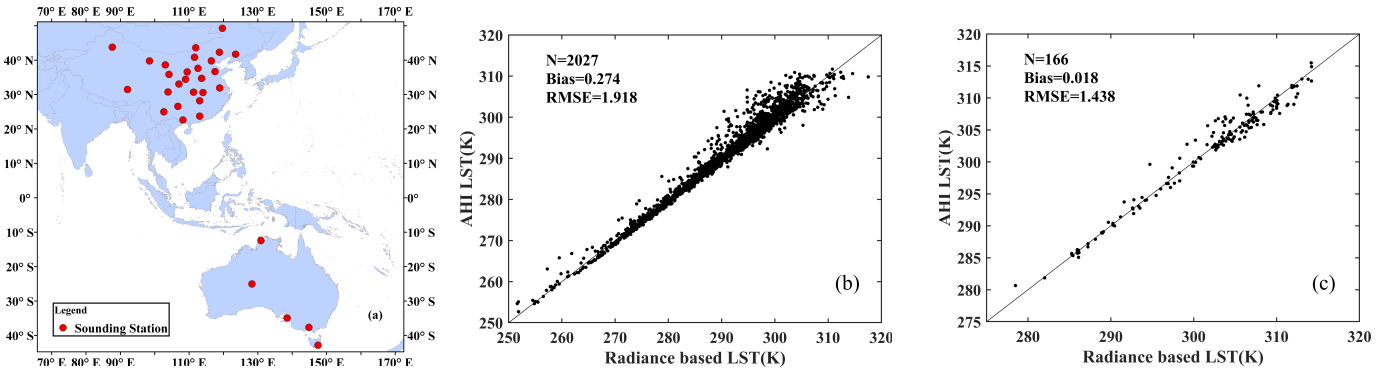

Fig. 13. (a) Locations of 31 sounding stations in China and Australia, and the corresponding scatterplots of the AHI and R-based LSTs for (b) China and (c) Australia.

TABLE VI
INFORMATION ABOUT THE LOCATIONS OF THE SEVEN SELECTED LARGE INLAND LAKES

Name	Latitude	Longitude
Chaohu Lake	31.50	117.55
Fuxian Lake	24.57	102.88
Hongze Lake	33.28	118.72
Qinghai Lake	37.02	100.15
Selincuo Lake	31.78	89.08
Taihu	31.22	120.07
Dianchi Lake	24.85	102.72

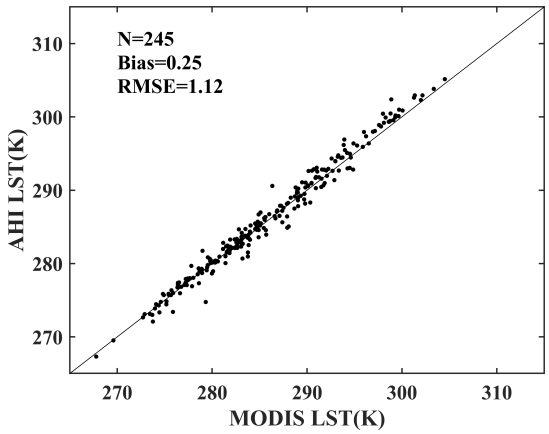

Fig. 14. Scatterplots of the AHI and MYD11L2 LSTs over the seven selected large inland lakes.

than 1.5 K for most cases compared to *in situ* measurements [85]. Moreover, the MOD21 LSEs are closer to the lab values than the MOD11 LSEs assigned based on classification schemes, especially over arid and semiarid areas. Therefore, the MYD21 V6 LST&E product is used for evaluation purposes [85].

As the spatial resolution of the AHI (0.02°) is coarser than that of MODIS (1 km), the MODIS LST&E is first aggregated to match the spatial resolution of the AHI. To reduce the influences of LST heterogeneity and pixel mismatch on the evaluation results, the following criteria are used to screen the mismatching LSTs:

1) The overpass time difference between AHI and MODIS must be less than five minutes.
2) The viewing zenith angle difference should meet the condition of $|\cos\theta_1/\cos\theta_2 - 1| < 0.01$, where θ_1 and θ_2 are the AHI and MODIS view zenith angles, respectively.
3) The MODIS pixels in the 7×7 window are clear-sky pixels, and the STD of the MODIS LST in the 3×3 window should be smaller than 2 K [5].

Fig. 15 shows the MODIS and AHI LSTs at 0445 UTC on January 3, 2016. The MODIS LST was retrieved for the northern region of Australia. The spatial distributions of the two LST products are similar, and the difference between the two LSTs is mostly smaller than 4 K. The bias and RMSE of this case are −0.24 and 2.64 K, respectively, compared with the MYD21 LST.

Fig. 16 shows the MODIS and AHI LSTs at 0600 UTC on January 25, 2016. The MODIS LST was retrieved for the center of China. The spatial distributions of the two LST products are similar, and the difference between the two LSTs is mostly smaller than 3 K. The bias and RMSE of this case are 0.36 and 1.7 K, respectively, compared with the MYD21 LST.

Fig. 17 shows the MODIS and AHI LSTs at 0555 UTC on July 28, 2016. The MODIS LST was retrieved for the center of China. The spatial distributions of the two LST products are similar, and the difference between the two LSTs is mostly smaller than 4 K. The bias and RMSE of this case are −0.57 and 2.36 K, respectively, compared with the MYD21 LST.

According to the LST evaluation results mentioned above, the AHI and MODIS LSTs are spatially consistent, and the differences reach 4 K under most conditions. The LST RMSE is 1.7 K in winter, while the value is 2.64 K in summer. The AHI and MODIS LSTs are more consistent in winter than in summer. There are two possible reasons for this phenomenon. First, the solar radiation is more intense in summer, which results in rapid surface heating in the daytime and an increase in LST heterogeneity. Second, the atmospheric moisture content is lower in winter, reducing the uncertainty of atmospheric correction.

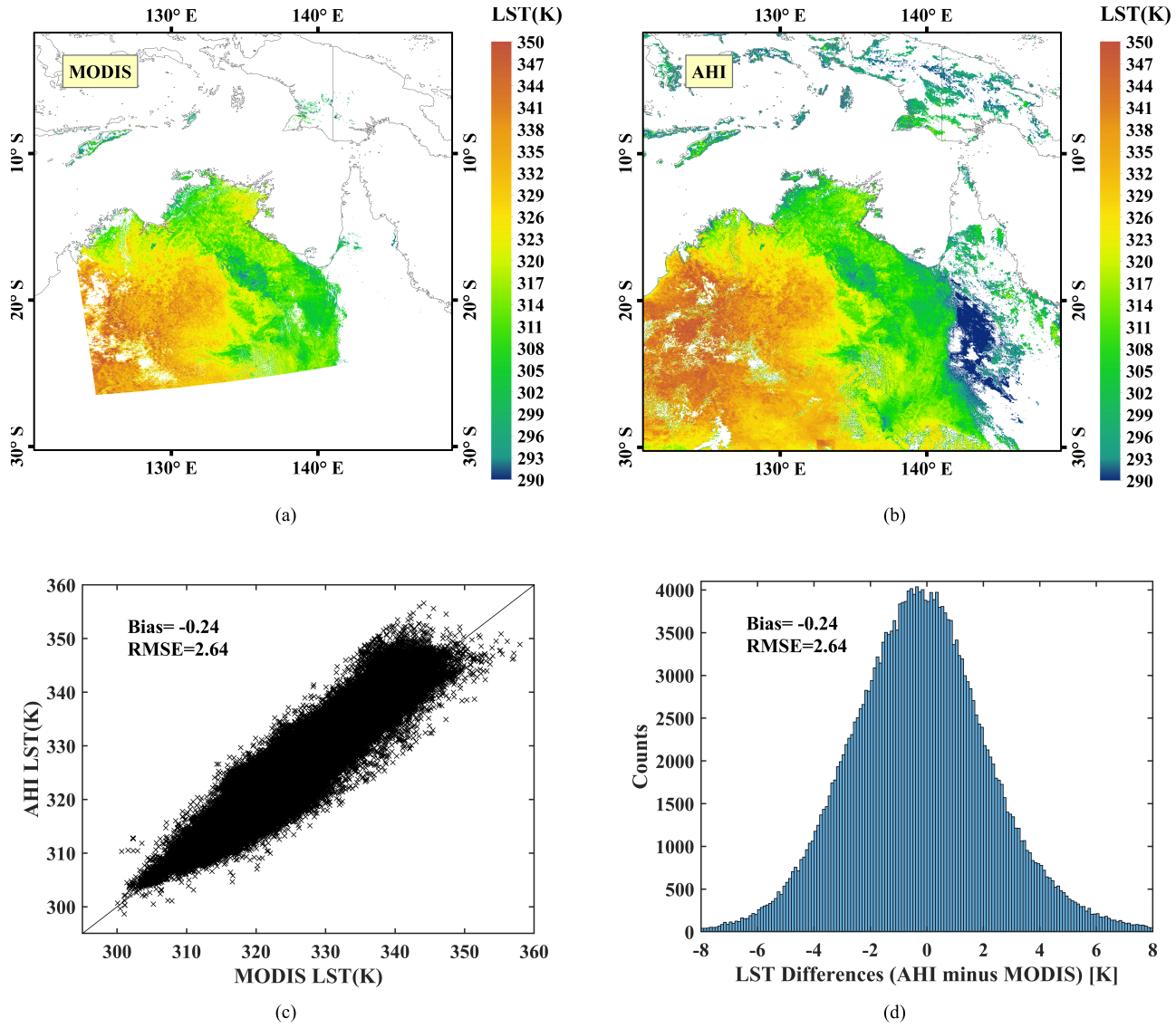

Fig. 15. Comparison of the AHI (January 3, 2016, 0440 UTC) and MYD21 (January 3, 2016, 0445 UTC) LSTs in the northern region of Australia. (a) LST spatial distribution of MODIS. (b) LST spatial distribution of the AHI. (c) Scatterplot of the AHI LST versus the MYD21 LST. (d) Histogram of the LST differences.

E. LSE Evaluation

Fig. 18 shows the MYD21 L2 LSE (August 11, 2016, 0555 UTC) and the AHI LSE at 0600 UTC on August 11, 2016. The AHI LSE was retrieved for Australia. The spatial distributions of the two LSE products are similar, and the difference between the two LSEs is mostly smaller than 0.01. The bias and RMSE of this case are −0.005 and 0.014, respectively, for AHI band 11; 0.004 and 0.006, respectively, for AHI band 14; and −0.004 and 0.006, respectively, for AHI band 15 compared with the MYD21 LSE.

V. Discussion

A. Effect of MMD Calibration

In Section III, we used the 4SAIL model to generate the canopy directional emissivity spectra to incorporate the cavity effect and calibrate the empirical relationship between $\varepsilon_{\min}$ and MMD for vegetated surfaces. The differences between the calibrated and original empirical relationships in regard to the TES algorithm over vegetated surfaces are further discussed in this section.

Four built-in atmospheric profiles in MODTRAN (namely, middle-latitude winter, US standard 1976, middle-latitude summer, and tropical) are used to generate the atmospheric downwelling radiation using MODTRAN 5.2. The LST–air temperature ranges from −10 to 20 K with an interval of 5 K. The emissivity spectra used are the same as those used in Section II. Note that instrument noise and atmospheric downwelling radiance errors are not considered here because we are only focused on comparing the performance of the calibrated empirical relationship. Finally, we obtain 3444 samples. The calibrated and original empirical relationships are used to retrieve the LSE and LST from the simulated data. The results are shown in Figs. 19 and 20. Fig. 19 reveals that the original empirical relationship underestimates the LSE by nearly 0.004 compared to the calibrated empirical relationship.

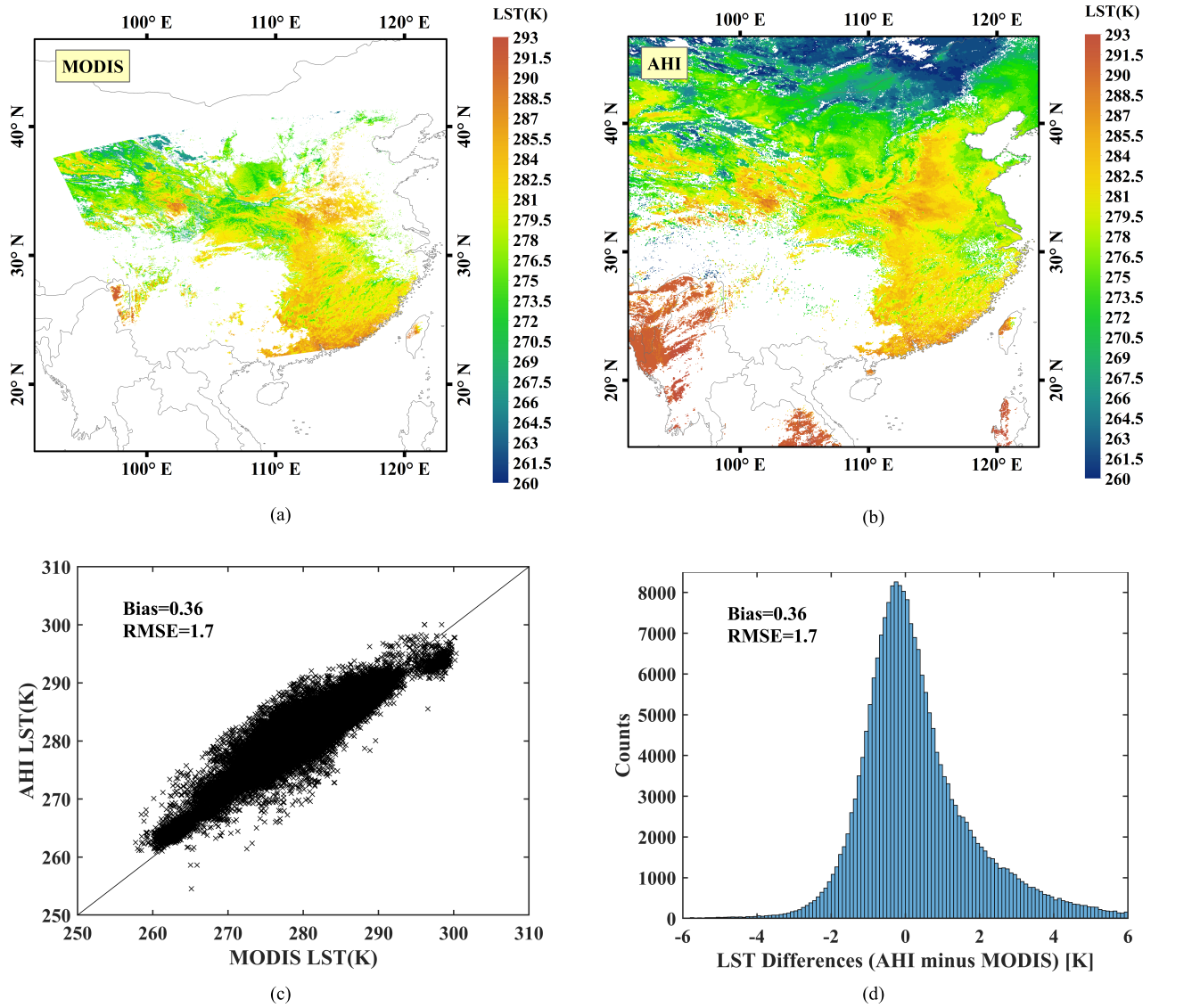

Fig. 16. Comparison of the AHI (January 25, 2016, 0600 UTC) and MODIS MYD21 (January 25, 2016, 0600 UTC) LSTs over China. (a) LST spatial distribution of MODIS. (b) LST spatial distribution of the AHI. (c) Scatterplot of the AHI LST versus the MYD21 LST. (d) Histogram of the LST differences.

Regarding the LST, the LST bias and RMSE of the original empirical relationship are 0.214 and 0.403 K, respectively, whereas those of the calibrated empirical relationship are 0.049 and 0.302 K, respectively (Fig. 20). Clearly, the calibrated empirical relationship improves the accuracy of LST retrieval. In summary, the calibrated empirical relationship improved the LST and LSE retrieval accuracy by up to 0.165 K and 0.004, respectively. Of course, only simulated data were used in this study, and field measurements will be collected in future studies to further verify the effect of the calibrated empirical relationship.

B. Effect of the Modified WVS Algorithm

The WVS algorithm was first proposed by Tonooka [43] in 2001. Initially, the WVS algorithm was only applicable to graybody pixels, and the WVS factor of the nongraybody pixels is interpolated by the scaling factor of the graybody pixels (named the WVS_interp algorithm). A refined WVS algorithm was proposed by Islam *et al.* [16], and the WVS algorithm was extended to nongraybody pixels (named the refined WVS algorithm). The modified WVS algorithm used in this article is similar to that in [16]. Hulley *et al.* [42] discussed the LST&E uncertainties in the TES algorithm under different atmospheric conditions, as well as the role of WVS algorithms in reducing uncertainties. Readers can refer to [42] for detailed information. This section focuses on the differences between the two WVS algorithms and the scope of their application.

To compare the performance of the WVS interpolation algorithm and the modified WVS algorithm, MODTRAN 5.2 is used to generate simulated data. To ensure generalization of the simulated data, representative atmospheric profiles at the global scale and LSE spectra representing a wide variety of surface types are used in the simulation. In addition, random instrument noise and atmospheric profile errors are added to the simulated data.

In total, 480 atmospheric profiles are randomly extracted from SeeBor, with a wide range of TPWs evenly distributed

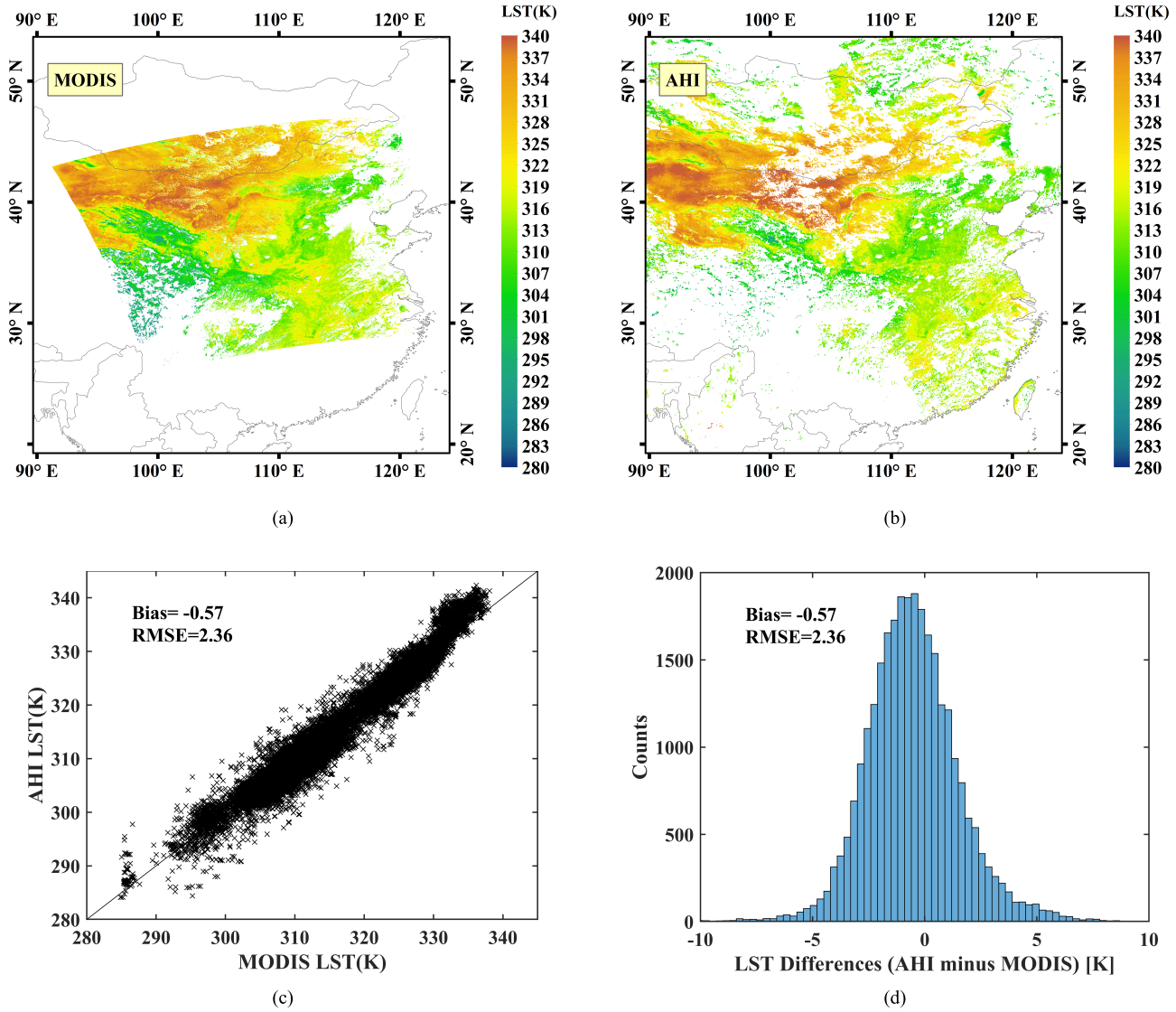

Fig. 17. Comparison of the AHI (July 28, 2016, 0550 UTC) and MYD21 (July 28, 2016, 0555 UTC) LSTs over China. (a) LST spatial distribution of MODIS. (b) LST spatial distribution of the AHI. (c) Scatterplot of the AHI LST versus the MYD21 LST. (d) Histogram of the LST differences.

over six subranges: [0,1], [1,2], [2,3], [3,4], [4,5], and [5,7] g/cm^2. To characterize the error of the atmospheric profile, a 2-K error is added to the air temperature profile above 700 hPa, and the error added to the layers below 700 hPa increases linearly from 2 K in the 700-hPa pressure layer to 4 K in the surface layer. The water vapor profile is scaled from 0.8 to 1.2. The LST is simulated using the ground air temperature with a mean air temperature of +3 K and an STD of 9 K. The emissivity spectra are extracted from the MODIS and ASTER spectral libraries, and similar spectra were removed by the spectral angle method. In total, 56 emissivity spectra are obtained, including vegetation, snow, ice, soil, and sand. The simulated data were constructed for five viewing angles (0°, 11.6°, 26.1°, 40.3°, and 53.7°).

The modified WVS algorithm needs the emissivity background value to determine the EMC/WVD coefficient, while the WVS interpolation algorithm needs graybody pixels to calculate and interpolate the WVS factor. In consideration of the above conditions, we need to simulate the TOA radiance for various LST&E values first. In addition, the TOA radiance of nearby graybody pixels and background LSE with an error should be included when constructing the simulated data. The simulated data are constructed as follows.

1) The atmospheric parameters $\tau_\lambda(\theta)$, $L_\lambda^{\uparrow}(\theta)$, and $L_\lambda^{\downarrow}$ are calculated using atmospheric profiles without errors, and $L_\lambda(\theta)$ is calculated using perfect atmospheric parameters under various LST&E conditions.
2) The adjusted atmosphere parameters $\tau_\lambda'(\theta)$, $L_\lambda^{\uparrow}(\theta)'$, and $L_\lambda^{\downarrow\prime}$ are calculated using adjusted air temperature and water vapor profiles.
3) Atmospheric parameters for scaled atmosphere profiles as in (2), but with the water vapor profile adjusted by a scaling factor (0.7), are calculated.
4) $L_\lambda^{\uparrow}(\theta)$ is calculated using the perfect atmospheric profile for a graybody surface type, which can be used by the WVS interpolation algorithm to calculate the WVS factor.

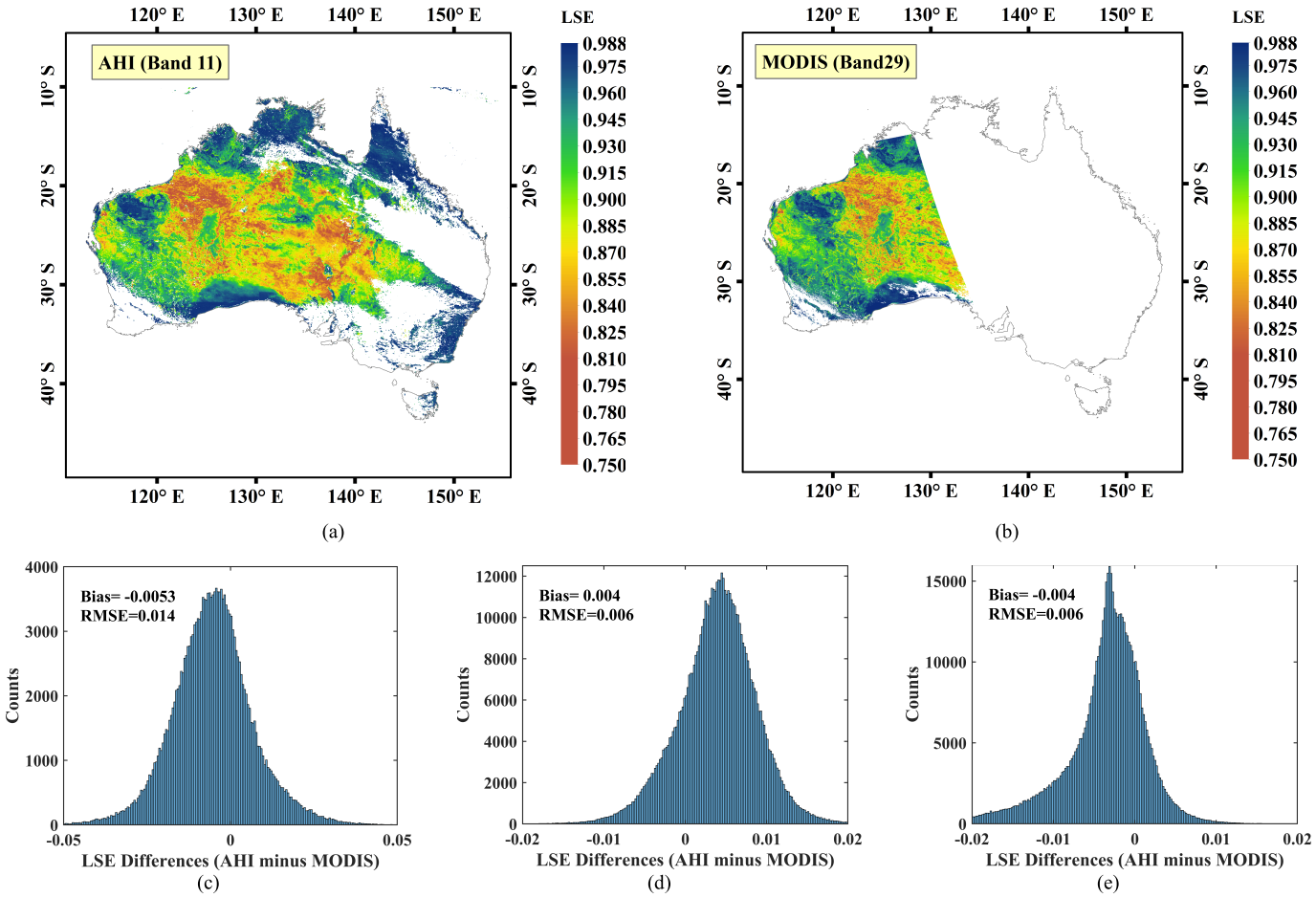

Fig. 18. Comparison of the AHI emissivity map (August 11, 2016, 0600 UTC) (a) AHI band 11 and the MYD21 LSE map (August 11, 2016, 0555 UTC) in Australia and (b) MODIS band 29 and the corresponding histogram of the LSE differences for AHI bands (c) 11, (d) 14, and (e) 15.

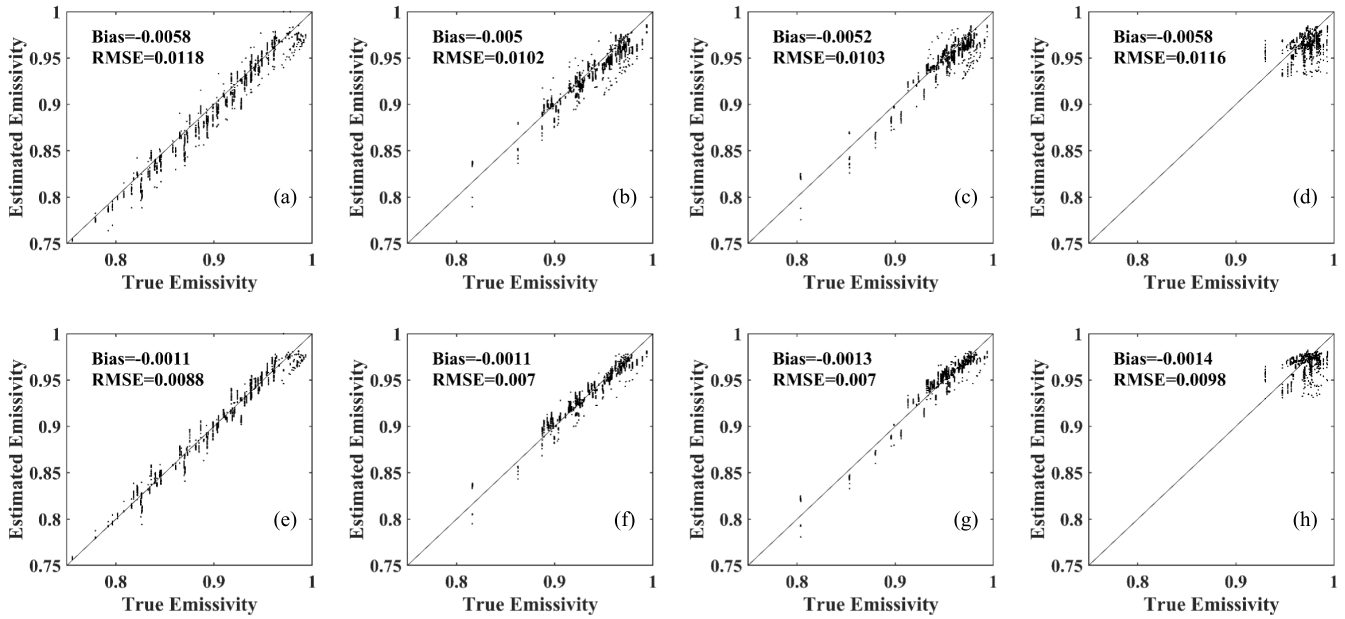

Fig. 19. Comparison of the true LSE with the LSEs derived using the calibrated and original empirical relationships from the simulated data set. (Top) Original empirical relationship. (Bottom) Calibrated empirical relationship. (a) and (e) Band 11. (b) and (f) Band 13. (c) and (g) Band 14. (d) and (h) Band 15.

5) An error of 0.01 is added to each band emissivity as the background emissivity value for the modified WVS algorithm. Finally, 0.2-K random noise is added to each band of the simulated TOA radiance.

In total, 144 000 samples are created. These samples are used to test the modified WVS and WVS_interp algorithms. LSEs with a band emissivity lower than 0 or higher than 1 are rejected because the TES algorithm cannot converge due to

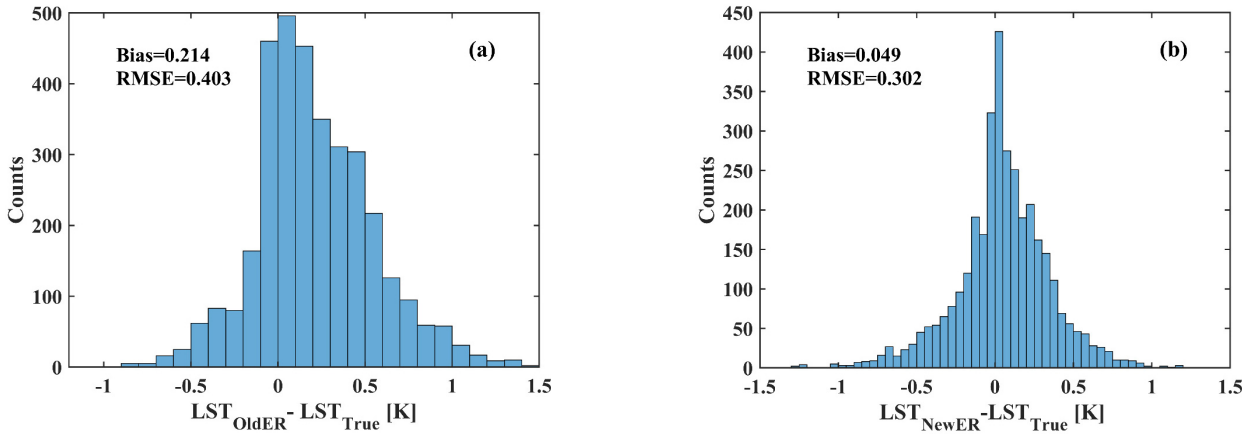

Fig. 20. Histogram of the LST differences between the TES retrievals and the validation data set. (Left) Original empirical relationship. (Right) Calibrated empirical relationship.

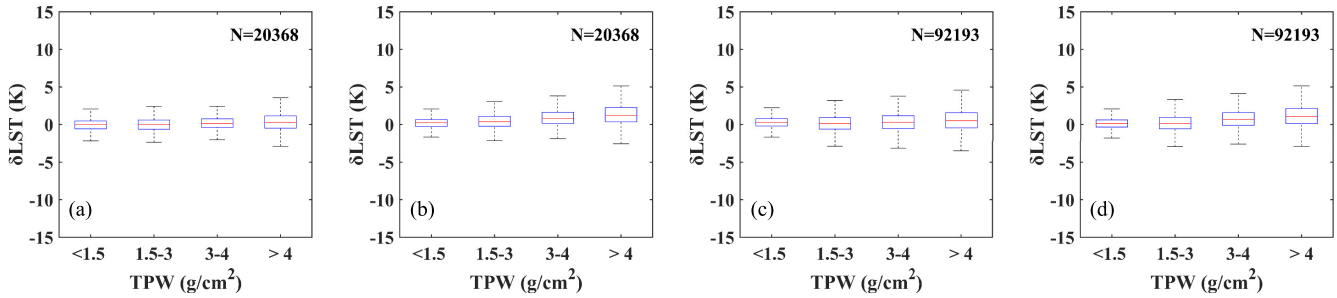

Fig. 21. Uncertainty boxplots of the AHI LST derived with the modified WVS algorithm and WVS_interp algorithm. (a) Graybody (Modified WVS + TES). (b) Graybody (WVS_{interp} + TES). (c) Nongraybody (Modified WVS + TES). (d) Nongraybody (WVS_{interp} + TES).

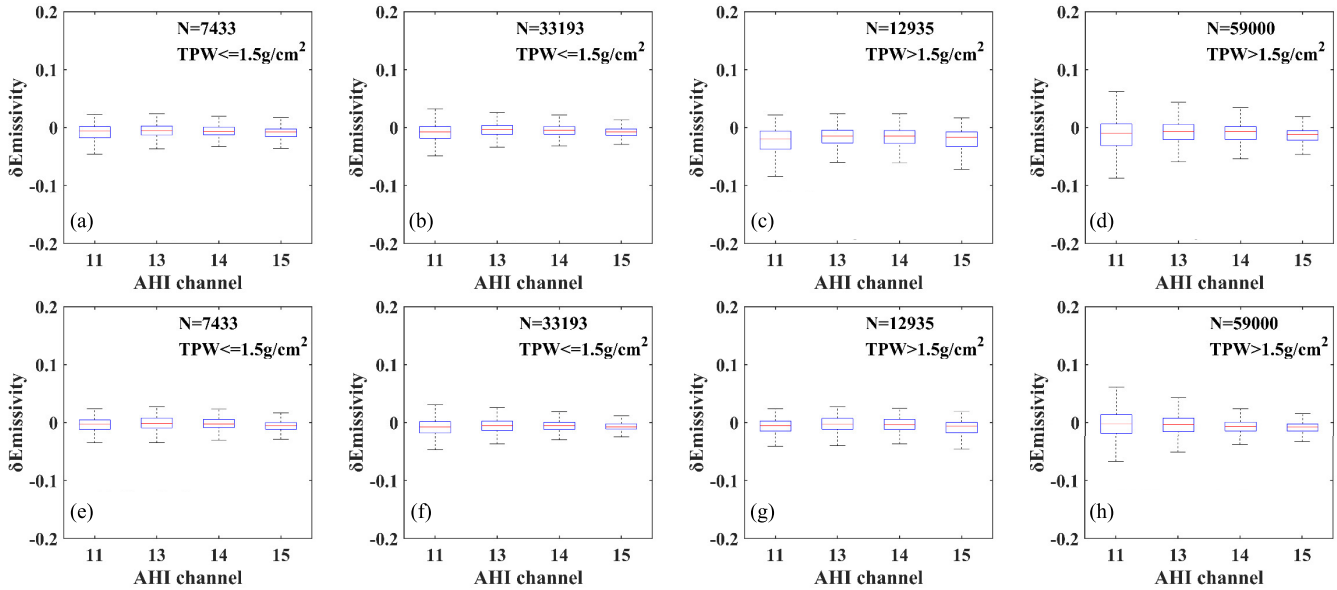

Fig. 22. Uncertainty boxplots of the AHI LSE derived with the modified WVS algorithm and WVS_interp algorithm. (a) and (c) Graybody (WVS_{interp} + TES). (b) and (d) Nongraybody (WVS_{interp} + TES). (e) and (g) Graybody (Modified WVS + TES). (f) and (h) Nongraybody (Modified WVS + TES).

incomplete atmospheric correction. Finally, 112 561 samples remain, and the results are summarized in Tables VII and VIII and shown in Figs. 21 and 22. The accuracy of the LST decreases with increasing water vapor for both the modified WVS and WVS_interp algorithms. The RMSE increases from 0.82 (TPW $<$ 1.5 g/cm^2) to 1.94 K (TPW $>$ 1.5 g/cm^2) for modified WVS algorithm, whereas the RMSE increases from 0.77 (TPW $<$ 1.5 g/cm^2) to 2.217 K (TPW $>$ 1.5 g/cm^2) for

TABLE VII
ACCURACY OF THE AHI LST RETRIEVED FROM THE MODIFIED WVS ALGORITHM AND ORIGINAL WVS_INTERP ALGORITHM UNDER DIFFERENT TPW CONDITIONS

Algorithm	Indices	TPW(g/cm^2)			
		<1.5	1.5-3	3-4	>4
M-WVS+TES	Bias	0.211	0.172	0.355	0.603
	RMSE	0.820	1.178	1.451	1.943
WVS_interp+TES	Bias	0.145	0.302	0.833	1.197
	RMSE	0.770	1.258	1.642	2.217

TABLE VIII
ACCURACY OF THE AHI LSE RETRIEVED FROM THE MODIFIED WVS ALGORITHM AND ORIGINAL WVS_INTERP ALGORITHM UNDER DIFFERENT TPW CONDITIONS

Algorithm	Band	TPW(g/cm^2)			
		<1.5	1.5-3	3-4	>4
M-WVS+TES	Band 11	-0.008(0.018)	-0.010(0.031)	-0.003(0.032)	-0.001(0.034)
	Band 13	-0.004(0.013)	-0.005(0.018)	-0.005(0.024)	-0.005(0.027)
	Band 14	-0.005(0.011)	-0.006(0.017)	-0.007(0.021)	-0.008(0.022)
	Band 15	-0.007(0.011)	-0.010(0.017)	-0.009(0.017)	-0.013(0.022)
WVS_interp+TES	Band 11	-0.009(0.019)	-0.016(0.033)	-0.018(0.041)	-0.016(0.042)
	Band 13	-0.004(0.012)	-0.008(0.021)	-0.013(0.030)	-0.015(0.034)
	Band 14	-0.005(0.011)	-0.010(0.021)	-0.015(0.030)	-0.017(0.034)
	Band 15	-0.008(0.013)	-0.015(0.022)	-0.015(0.022)	-0.019(0.028)

WVS_interp algorithm. Under the same water vapor conditions, the overall accuracy of graybody pixels is higher than that of nongraybody pixels for the modified WVS algorithm, but the decrease in accuracy is not significant. This proves that the modified WVS algorithm used in this article is effective for both graybody and nongraybody pixels, and the accuracy of the modified WVS algorithm is comparable to that of the original WVS_interp algorithm.

Compared with the original WVS_interp algorithm, the modified WVS algorithm expands the application scope of the WVS algorithm, although there is no essential difference between these two algorithms. For example, the modified WVS algorithm can calculate the WVS factor for all pixels without interpolation; however, the interpolation method can also be included in the modified WVS algorithm when the quality of the background emissivity cannot be guaranteed and there are graybodies such as vegetation in the surrounding pixels. In addition, for arid and semiarid areas without nearby graybody pixels, the modified WVS is superior to the original WVS_interp algorithm, especially under the condition of a high water vapor content.

VI. CONCLUSION

The LST is a vital physical parameter that characterizes the land surface processes and is a direct driving factor for the surface–atmosphere energy exchange. Clearly, the AHI does not provide an operational LST product. We developed an improved TES algorithm for estimating the LST&E from Himawari-8/AHI data in this study. First, a modified WVS algorithm is developed to improve the performance of atmospheric correction. Then we recalibrate the empirical relationship over vegetated surfaces in the original TES algorithm using the simulated directional emissivity spectra generated by the canopy radiative transfer model (4SAIL), in which the cavity effect is explicitly incorporated. According to the simulation study, the recalibrated empirical relationship improved the LST and LSE retrieval accuracies over vegetate surfaces by up to 0.165 and 0.004 K, respectively.

The WVS algorithm was extended to nongraybody pixels by fitting the coefficients of the EMC/WVD algorithm according to the minimum emissivity of the AHI bands. Simulation studies revealed that the accuracy of the modified WVS algorithm is comparable to that of the original WVS algorithm in deriving the LST and LSE. The merit of the modified WVS algorithm is that the application scope of the WVS algorithm is expanded.

Comprehensive validation and evaluation are conducted in this study. The improved TES algorithm is then used to derive LST and LSE from one-year-old AHI data in 2016. *In situ* measurements collected from the HiWATER, BSRN, and OzFlux networks are used for T-based validation. According to the validation results, the bias and RMSE are 0.19 and 2.93 K, respectively, in the daytime, and −0.43 and 1.95 K, respectively, in the nighttime. The accuracy of the AHI is higher in the nighttime than that in the daytime, due to the lower heterogeneity of the surface temperature in the nighttime. We also conduct R-based LST validation. The bias and RMSE are 0.25 and 1.88 K, respectively. Additionally, the derived AHI LST is evaluated using the MYD11 LST over homogeneous large inland lakes, the bias and RMSE are 0.25 and 1.12 K, respectively.

The derived AHI LST and LSE are first evaluated by MYD21 LST and LSE products, respectively. The spatial distributions of the two LST products are quite similar, and the difference between the two LSTs is mostly smaller than 4 K. The bias and RMSE of the LST differences (AHI minus MODIS) range from −0.57 to 0.36 K, and from 1.7 to 2.64 K, respectively. When compared to the MYD21 LSE product, the biases and RMSEs are smaller than 0.005 and 0.014 for the three AHI bands.

According to the validation and evaluation results, we can conclude that the improved TES algorithm can be used to accurately derive LST&E from AHI data. This study will certainly facilitate the usage of AHI TIR data and benefit the research of surface energy balance and climate change.

REFERENCES

[1] H. Mannstein, "Surface energy budget, surface temperature and thermal inertia," in *Remote Sensing Applications in Meteorology and Climatology*. Dordrecht, The Netherlands: Springer, 1987, pp. 391–410.

[2] R. G. Allen, M. Tasumi, and R. Trezza, "Satellite-based energy balance for mapping evapotranspiration with internalized calibration (METRIC)—Model," *J. Irrigation Drainage Eng.*, vol. 133, no. 4, pp. 380–394, 2007.

[3] B. Bond-Lamberty and A. Thomson, "Temperature-associated increases in the global soil respiration record," *Nature*, vol. 464, no. 7288, pp. 579–582, Mar. 2010.

[4] Y.-Y. Choi and M.-S. Suh, "Development of Himawari-8/Advanced Himawari Imager (AHI) Land Surface Temperature retrieval algorithm," *Remote Sens.*, vol. 10, no. 12, p. 2013, 2018.

[5] G.-M. Jiang and W.-X. Li, "Land Surface Temperature retrieval from the infrared measurements of Advanced Himawari Imager on Himawari-8," in *Proc. IEEE Int. Geosci. Remote Sens. Symp. (IGARSS)*, Jul. 2018, pp. 2535–2538.

[6] P. Schneider *et al.*, "Satellite observations indicate rapid warming trend for lakes in California and Nevada," *Geophys. Res. Lett.*, vol. 36, no. 22, 2009, Art. no. L22402, doi: 10.1029/2009GL040846.

[7] G. R. Diak and M. S. Whipple, "Improvements to models and methods for evaluating the land-surface energy balance and 'effective' roughness using radiosonde reports and satellite-measured 'skin' temperature data," *Agricult. Forest Meteorol.*, vol. 63, nos. 3–4, pp. 189–218, Mar. 1993.

[8] J. M. Norman, M. Divakarla, and N. S. Goel, "Algorithms for extracting information from remote thermal-IR observations of the Earth's surface," *Remote Sens. Environ.*, vol. 51, no. 1, pp. 157–168, 1995.

[9] L. M. Mcmillin, "Estimation of sea surface temperatures from two infrared window measurements with different absorption," *J. Geophys. Res.*, vol. 80, no. 36, pp. 5113–5117, Dec. 1975.

[10] Z. Qin, A. Karnieli, and P. Berliner, "A mono-window algorithm for retrieving land surface temperature from Landsat TM data and its application to the Israel-Egypt border region," *Int. J. Remote Sens.*, vol. 22, no. 18, pp. 3719–3746, Jan. 2001.

[11] J. C. Jiménez-Muñoz and J. A. Sobrino, "A generalized single-channel method for retrieving land surface temperature from remote sensing data," *J. Geophys. Res., Atmos.*, vol. 108, no. D22, Nov. 2003.

[12] J. C. Jiménez-Muñoz, J. A. Sobrino, D. Skokovic, C. Mattar, and J. Cristobal, "Land surface temperature retrieval methods from Landsat-8 thermal infrared sensor data," *IEEE Geosci. Remote Sens. Lett.*, vol. 11, no. 10, pp. 1840–1843, Oct. 2014.

[13] A. Gillespie, S. Rokugawa, T. Matsunaga, J. S. Cothern, S. Hook, and A. B. Kahle, "A temperature and emissivity separation algorithm for Advanced Spaceborne Thermal Emission and Reflection Radiometer (ASTER) images," *IEEE Trans. Geosci. Remote Sens.*, vol. 36, no. 4, pp. 1113–1126, Jul. 1998.

[14] C. Coll *et al.*, "Temperature and emissivity separation from ASTER data for low spectral contrast surfaces," *Remote Sens. Environ.*, vol. 110, no. 2, pp. 162–175, Sep. 2007.

[15] T. Schmugge, A. French, J. C. Ritchie, A. Rango, and H. Pelgrum, "Temperature and emissivity separation from multispectral thermal infrared observations," *Remote Sens. Environ.*, vol. 79, nos. 2–3, pp. 189–198, Feb. 2002.

[16] T. Islam, G. C. Hulley, N. K. Malakar, R. G. Radocinski, P. C. Guillevic, and S. J. Hook, "A physics-based algorithm for the simultaneous retrieval of land surface temperature and emissivity from VIIRS thermal infrared data," *IEEE Trans. Geosci. Remote Sens.*, vol. 55, no. 1, pp. 563–576, Jan. 2016.

[17] B. Carli *et al.*, "First results of MIPAS/ENVISAT with operational level 2 code," *Adv. Space Res.*, vol. 33, no. 7, pp. 1012–1019, Jan. 2004.

[18] N. K. Malakar and G. C. Hulley, "A water vapor scaling model for improved land surface temperature and emissivity separation of MODIS thermal infrared data," *Remote Sens. Environ.*, vol. 182, pp. 252–264, Sep. 2016.

[19] F. Becker and Z.-L. Li, "Temperature-independent spectral indices in thermal infrared bands," *Remote Sens. Environ.*, vol. 32, no. 1, pp. 17–33, Apr. 1990.

[20] Z. Wan and Z.-L. Li, "A physics-based algorithm for retrieving land-surface emissivity and temperature from EOS/MODIS data," *IEEE Trans. Geosci. Remote Sens.*, vol. 35, no. 4, pp. 980–996, Jul. 1997.

[21] Z. Wan and J. Dozier, "A generalized split-window algorithm for retrieving land-surface temperature from space," *IEEE Trans. Geosci. Remote Sens.*, vol. 34, no. 4, pp. 892–905, Jul. 1996.

[22] J. A. Sobrino, Z.-L. Li, M. P. Stoll, and F. Becker, "Multi-channel and multi-angle algorithms for estimating sea and land surface temperature with ATSR data," *Int. J. Remote Sens.*, vol. 17, no. 11, pp. 2089–2114, Jul. 1996.

[23] D. Sun and R. T. Pinker, "Estimation of land surface temperature from a Geostationary Operational Environmental Satellite (GOES-8)," *J. Geophys. Res., Atmos.*, vol. 108, no. D11, 2003, Art. no. 4326, doi: 10.1029/2002JD002422.

[24] Y. Yamamoto, H. Ishikawa, Y. Oku, and Z. Hu, "An algorithm for land surface temperature retrieval using three thermal infrared bands of Himawari-8," *J. Meteorol. Soc. Jpn. II*, vol. 96B, pp. 59–76, 2018.

[25] X. Xu, L. Chen, and J. Zhuang, "Genetic inverse algorithm for retrieval of component temperature of mixed pixel by multi-angle thermal infrared remote sensing data," *Sci. China D, Earth Sci.*, vol. 44, no. 4, pp. 363–372, Apr. 2001.

[26] J. Cheng, Q. Liu, X. Li, Q. Xiao, Q. Liu, and Y. Du, "Correlation-based temperature and emissivity separation algorithm," *Sci. China D, Earth Sci.*, vol. 51, no. 3, pp. 357–369, Mar. 2008.

[27] S. Zhou and J. Cheng, "A multi-scale wavelet-based temperature and emissivity separation algorithm for hyperspectral thermal infrared data," *Int. J. Remote Sens.*, vol. 39, no. 22, pp. 8092–8112, Nov. 2018.

[28] J. Cheng, S. Liang, J. Wang, and X. Li, "A stepwise refining algorithm of temperature and emissivity separation for hyperspectral thermal infrared data," *IEEE Trans. Geosci. Remote Sens.*, vol. 48, no. 3, pp. 1588–1597, Mar. 2009.

[29] N. Wang, H. Wu, F. Nerry, C. Li, and Z.-L. Li, "Temperature and emissivity retrievals from hyperspectral thermal infrared data using linear spectral emissivity constraint," *IEEE Trans. Geosci. Remote Sens.*, vol. 49, no. 4, pp. 1291–1303, Apr. 2010.

[30] J. Li, J. Li, E. Weisz, and D. K. Zhou, "Physical retrieval of surface emissivity spectrum from hyperspectral infrared radiances," *Geophys. Res. Lett.*, vol. 34, no. 16, Aug. 2007, Art. no. L16812, doi: 10.1029/2007GL030543.

[31] M. Paul, F. Aires, C. Prigent, I. F. Trigo, and F. Bernardo, "An innovative physical scheme to retrieve simultaneously surface temperature and emissivities using high spectral infrared observations from IASI," *J. Geophys. Res., Atmos.*, vol. 117, no. D11, Jun. 2012, Art. no. D11302, doi: 10.1029/2011JD017296.

[32] Z. Wan, "New refinements and validation of the collection-6 MODIS land-surface temperature/emissivity product," *Remote Sens. Environ.*, vol. 140, pp. 36–45, Jan. 2014.

[33] P. C. Guillevic *et al.*, "Validation of Land Surface Temperature products derived from the Visible Infrared Imaging Radiometer Suite (VIIRS) using ground-based and heritage satellite measurements," *Remote Sens. Environ.*, vol. 154, pp. 19–37, Nov. 2014.

[34] C. Gao, B.-H. Tang, H. Wu, X. Jiang, and Z.-L. Li, "A generalized split-window algorithm for land surface temperature estimation from MSG-2/SEVIRI data," *Int. J. Remote Sens.*, vol. 34, no. 12, pp. 4182–4199, Jun. 2013.

[35] B. Tang, Y. Bi, Z.-L. Li, and J. Xia, "Generalized split-window algorithm for estimate of land surface temperature from Chinese geostationary FengYun Meteorological Satellite (FY-2C) data," *Sensors*, vol. 8, no. 2, pp. 933–951, 2008.

[36] G.-M. Jiang, W. Zhou, and R. Liu, "Development of split-window algorithm for land surface temperature estimation from the VIRR/FY-3A measurements," *IEEE Geosci. Remote Sens. Lett.*, vol. 10, no. 4, pp. 952–956, Jul. 2013.

[37] Y. Yu *et al.*, "Developing algorithm for operational GOES-R land surface temperature product," *IEEE Trans. Geosci. Remote Sens.*, vol. 47, no. 3, pp. 936–951, Mar. 2008.

[38] K. Bessho, K. Date, M. Hayashi, A. Ikeda, T. Imai, and H. Inoue, "An introduction to Himawari-8/9—Japan's new-generation geostationary meteorological satellites," *J. Meteorol. Soc. Jpn. II*, vol. 94, no. 2, pp. 151–183, 2016.

[39] S.-B. Duan, Z.-L. Li, J. Cheng, and P. Leng, "Cross-satellite comparison of operational land surface temperature products derived from MODIS and ASTER data over bare soil surfaces," *ISPRS J. Photogramm. Remote Sens.*, vol. 126, pp. 1–10, Apr. 2017.

[40] H. Li *et al.*, "Comparison of the MuSyQ and MODIS Collection 6 land surface temperature products over barren surfaces in the Heihe River Basin, China," *IEEE Trans. Geosci. Remote Sens.*, vol. 57, no. 10, pp. 8081–8094, Oct. 2019.

[41] H. Li *et al.*, "Evaluation of the VIIRS and MODIS LST products in an arid area of Northwest China," *Remote Sens. Environ.*, vol. 142, pp. 111–121, Feb. 2014.

[42] G. C. Hulley, C. G. Hughes, and S. J. Hook, "Quantifying uncertainties in land surface temperature and emissivity retrievals from ASTER and MODIS thermal infrared data," *J. Geophys. Res., Atmos.*, vol. 117, no. D23, Dec. 2012, Art. no. D23113, doi: 10.1029/2012JD018506.

[43] H. Tonooka, "An atmospheric correction algorithm for thermal infrared multispectral data over land—A water-vapor scaling method," *IEEE Trans. Geosci. Remote Sens.*, vol. 39, no. 3, pp. 682–692, Mar. 2001.

[44] H. Tonooka, "Accurate atmospheric correction of ASTER thermal infrared imagery using the WVS method," *IEEE Trans. Geosci. Remote Sens.*, vol. 43, no. 12, pp. 2778–2792, Dec. 2005.

[45] H. Li *et al.*, "Evaluation of atmospheric correction methods for the ASTER temperature and emissivity separation algorithm using ground observation networks in the HiWATER experiment," *IEEE Trans. Geosci. Remote Sens.*, vol. 57, no. 5, pp. 3001–3014, May 2018.

[46] C. Coll, V. García-Santos, R. Niclos, and V. Caselles, "Test of the MODIS land surface temperature and emissivity separation algorithm with ground measurements over a rice paddy," *IEEE Trans. Geosci. Remote Sens.*, vol. 54, no. 5, pp. 3061–3069, May 2016.

[47] A. Berk *et al.*, "MODTRAN 5: A reformulated atmospheric band model with auxiliary species and practical multiple scattering options: Update," *Proc. SPIE*, vol. 5806, pp. 662–667, Jun. 2005.

[48] A. R. Gillespie *et al.*, "Temperature/emissivity separation algorithm theoretical basis document, version 2.4," NASA, Washington, DC, USA, ATBD Contract NAS5-31372, 1999.

[49] A. R. Gillespie, "Lithologic mapping of silicate rocks using TIMS," in *Proc. TIMS Data Workshop*. Pasadena, CA, USA: Jet Propulsion Lab, 1986, pp. 29–44.

[50] P. S. Kealy and S. J. Hook, "Separating temperature and emissivity in thermal infrared multispectral scanner data: Implications for recovering land surface temperatures," *IEEE Trans. Geosci. Remote Sens.*, vol. 31, no. 6, pp. 1155–1164, Nov. 1993.

[51] T. Matsunaga, "A temperature-emissivity separation method using an empirical relationship between the mean, the maximum, and the minimum of the thermal infrared emissivity spectrum," *J. Remote Sens. Soc. Jpn.*, vol. 14, no. 3, pp. 230–241, 1994.

[52] A. M. Baldridge, S. J. Hook, C. I. Grove, and G. Rivera, "The ASTER spectral library version 2.0," *Remote Sens. Environ.*, vol. 113, no. 4, pp. 711–715, Apr. 2009.

[53] F. Jacob *et al.*, "Reassessment of the temperature-emissivity separation from multispectral thermal infrared data: Introducing the impact of vegetation canopy by simulating the cavity effect with the SAIL-thermique model," *Remote Sens. Environ.*, vol. 198, pp. 160–172, Sep. 2017.

[54] A. Olioso, F. Jacob, and A. Lesaignoux, "SAIL-Thermique: A model for land surface spectral emissivity in the thermal infrared. Evaluation and reassesment of the temperature—Emissivity separation (TES) algorithm in presence of vegetation canopies," in *Proc. AGU Fall Meeting Abstr.*, 2014.

[55] W. Verhoef, L. Jia, Q. Xiao, and Z. Su, "Unified optical-thermal four-stream radiative transfer theory for homogeneous vegetation canopies," *IEEE Trans. Geosci. Remote Sens.*, vol. 45, no. 6, pp. 1808–1822, Jun. 2007.

[56] R. H. Yuhas, A. F. Goetz, and J. W. Boardman, "Discrimination among semi-arid landscape endmembers using the spectral angle mapper (SAM) algorithm," in *Proc. Summaries 3rd Annu. JPL Airborne Geosci. Workshop AVIRIS Workshop*. Pasadena, CA, USA: Colorado Univ., Jet Propulsion Laboratory, vol. 1, 1992, pp. 147–149.

[57] M. Momeni and M. Saradjian, "Evaluating NDVI-based emissivities of MODIS bands 31 and 32 using emissivities derived by Day/Night LST algorithm," *Remote Sens. Environ.*, vol. 106, no. 2, pp. 190–198, Jan. 2007.

[58] W. P. Elliott and D. J. Gaffen, "On the utility of radiosonde humidity archives for climate studies," *Bull. Amer. Meteorol. Soc.*, vol. 72, no. 10, pp. 1507–1520, Oct. 1991.

[59] R. Cullather and M. Bosilovich, "Climate data guide-modern era retrospective analysis for research and applications, version 2 (MERRA-2)," NASA Goddard Space Flight Center, Greenbelt, MD, USA, Tech. Rep. GSFC-E-DAA-TN48293, 2017.

[60] A. R. Gillespie, E. A. Abbott, L. Gilson, G. Hulley, J.-C. Jiménez-Muñoz, and J. A. Sobrino, "Residual errors in ASTER temperature and emissivity standard products AST08 and AST05," *Remote Sens. Environ.*, vol. 115, no. 12, pp. 3681–3694, Dec. 2011.

[61] G. C. Hulley, S. J. Hook, and C. Hughes, "MODIS MOD21 land surface temperature and emissivity algorithm theoretical basis document," Jet Propuls. Lab., Nat. Aeronaut. Space, Pasadena, CA, USA, Tech. Rep. JPL-Publ-12-17, Rev. 2, 2012.

[62] H. Tonooka, "Introduction of water vapor dependent coefficients to multichannel algorithms," *J. Remote Sens. Soc. Jpn.*, vol. 20, no. 2, pp. 137–148, 2000.

[63] A. Berk, L. S. Bernstein, and D. C. Robertson, "MODTRAN: A moderate resolution model for LOWTRAN," Spectral Sci. Inc., Burlington, MA, USA, Tech. Rep. GL-TR-89-0122, 1987.

[64] E. Borbas *et al.*, "Global profile training database for satellite regression retrievals with estimates of skin temperature and emissivity," in *Proc. 14th Int. ATOVS Study Conf.*, 2005, pp. 763–770.

[65] J. Chen *et al.*, "A simple method for reconstructing a high-quality NDVI time-series data set based on the Savitzky–Golay filter," *Remote Sens. Environ.*, vol. 91, nos. 3–4, pp. 332–344, 2004.

[66] E. Borbas, G. Hulley, M. Feltz, R. Knuteson, and S. Hook, "The combined ASTER MODIS emissivity over land (CAMEL) part 1: Methodology and high spectral resolution application," *Remote Sens.*, vol. 10, no. 4, p. 643, 2018.

[67] M. Feltz, E. Borbas, R. Knuteson, G. Hulley, and S. Hook, "The combined ASTER MODIS emissivity over land (CAMEL) part 2: Uncertainty and validation," *Remote Sens.*, vol. 10, no. 5, p. 664, 2018.

[68] R. Saunders *et al.*, "An update on the RTTOV fast radiative transfer model (currently at version 12)," *Geoscientific Model Develop.*, vol. 11, no. 7, pp. 2717–2737, 2018.

[69] H. Tonooka, S. Rokugawa, and T. Hoshi, "Simultaneous estimation of atmospheric correction parameters, surface temperature and spectral emissivity using thermal infrared multispectral scanner data," *J. Remote Sens. Soc. Jpn.*, vol. 17, no. 2, pp. 129–143, 1997.

[70] X. Li *et al.*, "Heihe watershed allied telemetry experimental research (HiWATER): Scientific objectives and experimental design," *Bull. Amer. Meteorol. Soc.*, vol. 94, no. 8, pp. 1145–1160, 2013.

[71] S. Liu *et al.*, "The heihe integrated observatory network: A basin-scale land surface processes observatory in China," *Vadose Zone J.*, vol. 17, no. 1, 2018, Art. no. 180072.

[72] A. Ohmura *et al.*, "Baseline surface radiation network (BSRN/WCRP): New precision radiometry for climate research," *Bull. Amer. Meteorol. Soc.*, vol. 79, no. 10, pp. 2115–2136, Oct. 1998.

[73] J. Beringer *et al.*, "An introduction to the Australian and New Zealand flux tower network-OzFlux," *Biogeosciences*, vol. 13, no. 21, pp. 5895–5916, 2016.

[74] J. Cheng, S. Liang, Y. Yao, and X. Zhang, "Estimating the optimal broadband emissivity spectral range for calculating surface longwave net radiation," *IEEE Geosci. Remote Sens. Lett.*, vol. 10, no. 2, pp. 401–405, Mar. 2012.

[75] F. Jacob, F. Petitcolin, T. Schmugge, É. Vermote, A. French, and K. Ogawa, "Comparison of land surface emissivity and radiometric temperature derived from MODIS and ASTER sensors," *Remote Sens. Environ.*, vol. 90, no. 2, pp. 137–152, Mar. 2004.

[76] G. C. Hulley, S. J. Hook, and A. M. Baldridge, "Validation of the North American ASTER Land Surface Emissivity Database (NAALSED) version 2.0 using pseudo-invariant sand dune sites," *Remote Sens. Environ.*, vol. 113, no. 10, pp. 2224–2233, Oct. 2009.

[77] Z. Xu *et al.*, "Intercomparison of surface energy flux measurement systems used during the HiWATER-MUSOEXE," *J. Geophys. Res., Atmos.*, vol. 118, no. 23, pp. 13140–13157, 2013.
[78] J. M. Blonquist, B. D. Tanner, and B. Bugbee, "Evaluation of measurement accuracy and comparison of two new and three traditional net radiometers," *Agricult. Forest Meteorol.*, vol. 149, no. 10, pp. 1709–1721, Oct. 2009.
[79] G. L. Stephens *et al.*, "An update on Earth's energy balance in light of the latest global observations," *Nature Geosci.*, vol. 5, no. 10, pp. 691–696, Oct. 2012.
[80] Z. Wan and Z. L. Li, "Radiance-based validation of the V5 MODIS land-surface temperature product," *Int. J. Remote Sens.*, vol. 29, nos. 17–18, pp. 5373–5395, Sep. 2008.
[81] S.-B. Duan, Z.-L. Li, H. Wu, P. Leng, M. Gao, and C. Wang, "Radiance-based validation of land surface temperature products derived from collection 6 MODIS thermal infrared data," *Int. J. Appl. Earth Observ. Geoinf.*, vol. 70, pp. 84–92, Aug. 2018.
[82] W. Yu, M. Ma, H. Yang, J. Tan, and X. Li, "Supplement of the radiance-based method to validate satellite-derived land surface temperature products over heterogeneous land surfaces," *Remote Sens. Environ.*, vol. 230, Sep. 2019, Art. no. 111188.
[83] G. C. Hulley and S. J. Hook, "A radiance-based method for estimating uncertainties in the atmospheric infrared sounder (AIRS) land surface temperature product," *J. Geophys. Res., Atmos.*, vol. 117, no. D20, Oct. 2012, Art. no. D20117, doi: 10.1029/2012JD018102.
[84] Z. Wan, Y. Zhang, Q. Zhang, and Z.-L. Li, "Validation of the land-surface temperature products retrieved from Terra Moderate Resolution Imaging Spectroradiometer data," *Remote Sens. Environ.*, vol. 83, nos. 1–2, pp. 163–180, Nov. 2002.
[85] G. Hulley, N. Malakar, and R. Freepartner, "Moderate Resolution Imaging Spectroradiometer (MODIS) land surface temperature and emissivity product (MxD21) algorithm theoretical basis document collection-6," *JPL Publication*, pp. 12–17, May 2016.

Shugui Zhou received the master's degree in cartography and geographical information engineering from Capital Normal University, Beijing, China, in 2016. He is pursuing the Ph.D. degree with Beijing Normal University, Beijing.

His research interests include thermal infrared hyperspectral remote sensing, retrieval and validation of land surface temperature and emissivity, and blending of remote-sensed land surface temperature.

Jie Cheng (Senior Member, IEEE) received the Ph.D. degree in cartography and remote sensing from the Institute of Remote Sensing Applications, Chinese Academy of Sciences, Beijing, China, in 2008.

He was a Post-Doctoral Fellow with the State Key Laboratory of Remote Sensing Science, Beijing Normal University, Beijing, from 2008 to 2010, an Assistant Research Scientist with the University of Maryland, College Park, MD, USA, from 2009 to 2010, and a Visiting Scientist with the Hydrology and Remote Sensing Laboratory, United States Department of Agriculture-Agricultural Research Service, Beltsville, MD, from 2017 to 2018. He is an Associate Professor with the State Key Laboratory of Remote Sensing Science, Faculty of Geographical Science, Beijing Normal University. He has authored over 40 SCI indexed peer-reviewed articles as the first and corresponding authors, seven book chapters, and two special issues of *Remote Sensing*. His main research interests include the estimation of land surface variables from satellite observations, radiative transfer modeling, and studies on surface energy balance.